

1  
2  
3  
4  
5  
6  
7  
8  
9  
10  
11  
12  
13  
14  
15  
16  
17  
18  
19  
20

**Deep-Learning-derived Planetary Boundary Layer Height from  
Conventional Meteorological Measurements**

Tianning Su<sup>1\*</sup>, Yunyan Zhang<sup>1</sup>

<sup>1</sup>Lawrence Livermore National Laboratory, Livermore, CA, USA

Submission to *Atmospheric Chemistry and Physics*

\*Correspondence to: [su10@llnl.gov](mailto:su10@llnl.gov)

21 **Abstract.** The planetary boundary layer (PBL) height (PBLH) is an important  
22 parameter for various meteorological and climate studies. This study presents a multi-  
23 structure deep neural network (DNN) model, which can estimate PBLH by integrating  
24 the morning temperature profiles and surface meteorological observations. The DNN  
25 model is developed by leveraging a rich dataset of PBLH derived from long-standing  
26 radiosonde records and augmented with high-resolution micro-pulse lidar and Doppler  
27 lidar observations. We assess the performance of the DNN with an ensemble of ten  
28 members, each featuring distinct hidden layer structures, which collectively yield a  
29 robust 27-year PBLH dataset over the Southern Great Plains from 1994 to 2020. The  
30 influence of various meteorological factors on PBLH is rigorously analyzed through  
31 the importance test. Moreover, the DNN model's accuracy is evaluated against  
32 radiosonde observations and juxtaposed with conventional remote sensing  
33 methodologies, including Doppler lidar, ceilometer, Raman lidar, and Micro-pulse  
34 lidar. The DNN model exhibits reliable performance across diverse conditions and  
35 demonstrates lower biases relative to remote sensing methods. In addition, the DNN  
36 model, originally trained over a plain region, demonstrates remarkable adaptability  
37 when applied to the heterogeneous terrains and climates encountered during the  
38 GoAmazon (Tropical Rainforest) and CACTI (Middle Latitude Mountain) campaigns.  
39 These findings demonstrate the effectiveness of deep learning models in estimating  
40 PBLH, enhancing our understanding of boundary layer processes with implications for  
41 enhancing the representation of PBL in weather forecasting and climate modeling.

42

## 43 **1 Introduction**

44 The Planetary Boundary Layer (PBL) is the atmosphere's lowest part, where the  
45 Earth's surface directly influences meteorological variables, impacting the climate  
46 system (Garratt, 1994; Kaimal and Finnigan, 1994). The PBL height (PBLH) is a  
47 meteorological factor that strongly influences surface-atmosphere exchanges of heat,  
48 moisture, and energy (Stull, 1988; Caughey, 1984; Holtslag and Nieuwstadt, 1986;  
49 Mahrt, 1999; Helbig et al., 2021; Guo et al., 2024; Beamesderfer et al., 2022). In  
50 addition, PBLH ~~is~~ is a crucial variable for monitoring and simulating surface pollutant  
51 behaviors since it determines the volume available for near-surface pollutant dispersion  
52 (Li et al., 2017; Su et al., 2024a; Tucker et al., 2009; Wang et al. 2020). Due to its  
53 impact on cloud evolution and the development of convective systems, PBLH is also a  
54 key parameter in numerical weather forecasts and climate ~~models~~ projections models  
55 (Deardorff, 1970; Kaimal et al. 1976; Menut et al., 1999; Park et al., 2001; Emanuel,  
56 1994; Guo et al., 2017, 2019; Lilly, 1968; Matsui et al., 2004).

57 Radiosonde (SONDE) remains the standard method for estimating PBLH, yet it is  
58 hampered by limitations in temporal frequency, restricting its ability to capture the  
59 whole diurnal cycle of PBL development (Stull, 1988; Seidel et al. 2010; Guo et al.  
60 2021; Liu and Liang, 2010). To overcome these challenges, there has been an increasing  
61 dependence on remote sensing techniques, especially lidar systems. These techniques  
62 capture atmospheric vertical information (e.g., aerosols, temperature, humidity, and  
63 wind) at high temporal and vertical resolutions, leading to remote sensing-based  
64 retrievals of PBLH (Menut et al., 1999; Kotthaus et al., 2023; Sawyer and Li, 2013;

65 Wang et al., 2023). The remote sensing systems, including Doppler lidar (Barlow et al.  
66 2011), ceilometer (Zhang et al. 2022), Raman lidar (Summa et al. 2013), and Micro-  
67 pulse lidar (Melfi et al., 1985), utilize laser-based technology to track PBLH diurnal  
68 evolutions, helping us understand the PBL ~~dynamics~~ evolutions (Cohn and Angevine,  
69 2000; Davis et al., 2000). In addition, wind profilers can estimate the PBLH using  
70 algorithms that analyze the signal-to-noise ratio from wind profiler data (Molod et al.  
71 2015; Solanki et al. 2022; Liu et al. 2019; Salmun et al. 2023; Bianco and Wilczak  
72 2002; Bianco et al. 2008; Tao et al. 2021).

73 However, the advancement in remote sensing for the estimation of PBLH  
74 challenges is still posing in bridging the results obtained by different remote sensing  
75 instruments with those obtained from the SONDE measurements (Zhang et al. 2022;  
76 Chu et al., 2019). Specifically, interpreting aerosol, turbulence, and moisture profiles  
77 derived from remote sensing techniques to determine PBLH bears inherent limitations  
78 due to the unstable signal-to-noise ratio (Kotthaus et al., 2023; Krishnamurthy et al.,  
79 2021). This issue is compounded by the different measurement methodologies and  
80 definitions employed by various remote sensing tools, leading to uncertainties when  
81 comparing their PBLH estimates to the retrievals derived from SONDE measurements  
82 (Zhang et al. 2022; Sawyer and Li, 2013).

83 As machine learning (ML) has shown potential in atmospheric science (McGovern  
84 et al., 2017; Gagne et al., 2019; Su et al. 2020a; Vassallo et al., 2020; Cadeddu et al.,  
85 2009; Molero et al. 2022), this technique presents a promising tool for refining the  
86 estimation of PBLH to resolve the inherent complexity and variability of PBL. For

87 example, several studies use ML to identify PBLH using thermodynamic profiles  
88 Atmospheric Emitted Radiance Interferometer (AERI) or using backscatter profiles  
89 from lidar~~PBL heights using thermodynamic profiles or backscatter profiles from Lidar~~  
90 ~~or Atmospheric Emitted Radiance Interferometer (AERI)~~, highlighting the ML's  
91 superiority over conventional techniques under different scenarios (Sleeman et al. 2020;  
92 ~~Krishnamurthy et al., 2021~~; Rieutord et al. 2021; Liu et al. 2022; Ye et al. 2021). For  
93 example~~Moreover~~, Li et al. (2023) applied an ML algorithm for retrieving PBLH under  
94 complex atmospheric conditions with account of the vertical distribution of aerosols.  
95 Krishnamurthy et al. (2021) incorporated a random forest model, along with machine  
96 learning, to use Doppler lidar data for the extraction of PBLH with better results  
97 compared to the results retrieved by traditional methods.

Formatted: Font: Not Italic, Font color: Text 1

Formatted: Font: Not Italic, Font color: Text 1

Formatted: Font: Not Italic

98 While existing ML methodologies have made great progress ~~marked progress~~ in  
99 estimating PBLH, these studies mainly focus on refining retrievals from remote sensing  
100 data, particularly lidar-based technologies. Thus, there is an inherent limitation to the  
101 applicability due to a reliance on specific remote sensing instruments. To address this  
102 issue, we aim to leverage and integrate the comprehensive field observations (i.e.,  
103 radiosonde and remote sensing techniques) to develop a deep learning model for direct  
104 PBLH estimation from conventional meteorological data. This strategy circumvents the  
105 limitations of relying on particular remote sensing technologies. Furthermore, our  
106 model employs an advanced deep neural network (DNN) approach (Sze et al. 2017;  
107 Schmidhuber, 2015; Nielsen, 2015; Pang et al. 2020), diverging from traditional ML  
108 methods like random forest. This deep learning model utilizes ensemble techniques.

Formatted: Font: Not Italic

109 constructing arrays of various structures and using their average for the final estimation.  
110 This approach method provides particular advantages in the context of complex and  
111 nonlinear processes (Ganaie et al. 2022; Mohammed and Kora. 2023). Ensemble DNN  
112 with multi-structure designs shows very strong flexibility and robustness, so it  
113 relatively performs better and has high stability across a wide range of conditions (Xue  
114 et al. 2020; Dong et al. 2020). ~~our model employs a multi-structure deep neural network~~  
115 ~~(DNN), diverging from traditional ML methods like random forest, to enhance its~~  
116 ~~adaptivity for PBLH estimations. This multi-structure DNN approach offers great~~  
117 ~~potential for wide applications under various meteorological conditions, as well as a~~  
118 ~~stable performance for both trained and untrained periods.~~ ~~This underscores facilitates~~  
119 the adaptability versatility of DNN as a tool for PBLH estimation, which can be utilized  
120 under different scenarios and locations.

121 By focusing on the interaction between surface meteorology and the PBL, this study  
122 introduces a DNN-based method to estimate the daytime evolution of PBLH from  
123 morning temperature profiles and surface meteorology. We evaluate the model's  
124 performance using extensive datasets over the Southern Great Plains (SGP) for a period  
125 spanning 27 years (1994-2020) and includes comparisons with PBLH estimations  
126 obtained from Doppler lidar, ceilometer, Raman lidar, and micro-pulse lidar.  
127 Furthermore, we explore the generalizability of the model to different geographic  
128 regions and climates, as tested during the field campaigns, e.g., Green Ocean Amazon  
129 (GoAmazon) and Cloud, Aerosol, and Complex Terrain Interactions (CACTI).

130

131 **2 Data and instruments**

132 **2.1 ARM Sites**

133 The Atmospheric Radiation Measurement (ARM) program, funded by the U.S.  
134 Department of Energy, has been employed at the Southern Great Plains (SGP) site in  
135 Oklahoma (36.607°N, 97.488°W), ~~situated 314 meters above mean sea level for several~~  
136 ~~decades~~. This study use comprehensive field observations at the SGP site during 1994  
137 to 2020. In addition to the SGP site, this study utilizes data from the ARM GoAmazon  
138 (3.213°S, 60.598°W) and ARM CACTI (32.126°S, 64.728°W) field campaigns to carry  
139 out independant tests for the deep learning model. Specificly, the GoAmazon  
140 campaign is located in the amazon tropical forests and provides rich field observations  
141 data during 2014-2015 ([Martin et al. 2016](#)). Meanwhile, the CACTI central site, at an  
142 elevation of 1141 meters within the Sierras de Córdoba Mountain range in north-central  
143 Argentina, offers the observations during the 2018-2019 period ([Varble et al. 2021](#)).  
144 Utilizing these comprehensive ARM datasets, our study includes thermodynamic  
145 profiles derived from radiosondes, data from the Active Remote Sensing of Clouds  
146 ([ARSCL](#), [Clothiaux et al. 2000, 2001](#); [Kollias et al. 2020](#)), in-situ surface flux  
147 measurements, and standard meteorological observations at the surface, as documented  
148 by Cook (2018) and Xie et al. (2010).

149 SONDE measurements at the ARM sites launch routinely several times a day and  
150 provide detailed information into the thermodynamic conditions of the atmosphere. The  
151 technical details of the ARM SONDE data are documented in Holdridge et al. (2011).  
152 Moreover, we use the surface meteorological parameters at the standard meteorological

Formatted: Font: Times New Roman, 12 pt

Formatted: Font: Times New Roman, 12 pt

Formatted: Font: Times New Roman, 12 pt

Formatted: Font: Times New Roman, 12 pt

Formatted: Font: Times New Roman, 12 pt

153 station. In-situ measurements at 2 meters above ground level provide data on  
154 temperature, relative humidity, and vapor pressure. Moreover, this study obtain the  
155 surface sensible and latent heat fluxes from the surface instruments (Wesely et al.,  
156 1995). In SGP, we use the best-estimate surface fluxes in the Bulk Aerodynamic Energy  
157 Balance Bowen Ratio (BAEBBR) product, which is derived from the measurements by  
158 Energy Balance Bowen Ratio (EBBR). Due to the availability, we utilize the surface  
159 fluxes from Quality Controlled Eddy CORrelation (QCECOR) datasets from CACTI  
160 and GoAmazon sites (Tang et al. 2019).

161

## 162 **2.2 Existing PBLH datasets over the ARM sites**

163 For analyzing PBLH, we have utilized a variety of datasets to get a full picture of  
164 PBLH derived from different instruments. These datasets are developed by using  
165 different methodologies and instruments and jointly offer a detailed information of  
166 PBLH under various meteorological conditions. Among these datasets, SONDE- and  
167 ceilometer-derived PBLH are available for all three sites, other datasets are only  
168 available over the SGP. The technique details for these datasets can be found in the  
169 corresponding publications or technique reports.

170 *(1) SONDE-derived PBLH by Liu and Liang (2010):*

171 PBLHs are retrieved using a method developed by Liu and Liang (2010), based on  
172 potential temperature gradients from SONDE. We focus on daytime data during 05:00–  
173 18:00 Local Time (LT), with a resampled vertical resolution of 5-hPa. The SONDE  
174 dataset is available at DOI: <https://doi.org/10.5439/1595321>.



175 (2) *Doppler Lidar-derived PBLH by Sivaraman and Zhang (2021):*

176 Doppler lidar PBLH estimates are derived using a vertical velocity variance method  
177 during 2010-2019 (Tucker et al., 2009; Lareau et al., 2018; Sivaraman and Zhang 2021).  
178 The dataset is available at DOI: <https://doi.org/10.5439/1726254>.

179 (3) *Combined MPL and SONDE PBLH by Su et al. (2020b):*

180 We utilize a PBLH dataset that merges lidar and SONDE measurements during  
181 1998-2023, ensuring vertical coherence and temporal continuity (Su et al. 2020b). An  
182 additional method for handling cloudy conditions is detailed in Su et al. (2022). The  
183 dataset is available at DOI: <https://doi.org/10.5439/2007149>.

184 (4) *Ceilometer-derived PBLH by Zhang et al. (2022):*

185 The Vaisala CL31 ceilometer, with a 7.7 km vertical range, provides detailed  
186 backscatter profiles used for PBLH estimation via gradient methods during 2011-2023  
187 (Zhang et al. 2022). Enhanced algorithms ensure robust estimations under all weather  
188 conditions. The dataset is available at DOI: <https://doi.org/10.5439/1095593>.

189 (5) *MPL-derived PBLH by Sawyer and Li (2013):*

190 Micropulse lidar (MPL) is utilized for its high temporal resolution to retrieve PBLH  
191 during 2009-2020. MPL-derived PBLH, validated against SONDE and ~~infrared~~  
192 ~~spectrometer~~ (AERI) data, improves understanding of boundary-layer processes  
193 (Sawyer and Li. 2013). The dataset is available at DOI:  
194 <https://doi.org/10.5439/1637942>.

195 (6) *Combined Raman Lidar and AERI PBLH by Ferrare (2012):*

196 PBLH is calculated using merged potential temperature profiles from Raman lidar  
197 and AERI, with criteria established for the SGP site. PBL heights are computed hourly  
198 for 2009-2011. The dataset is available at DOI: <https://doi.org/10.5439/1169501>.

199 In the datasets, (1-3) serve as the foundation for training. Concurrently, considering  
200 radiosonde as the benchmark standard, we utilized dataset (1) for validating PBLH  
201 retrievals obtained from various sources. Meanwhile, datasets (4-6) are used for the  
202 intercomparisons between PBLH derived from DNN and remote sensing techniques.

203

### 204 **3 Deep Learning Model to Estimate PBLH**

#### 205 **3.1 The Multi-Structure Deep Learning Model**

206 Our deep learning model for estimating PBLH leverages the robustness of ensemble  
207 learning using a multi-structure DNN (Sze et al. 2017; Schmidhuber, 2015; Nielsen,  
208 2015; Pang et al. 2020). This model used the TensorFlow Package, developed by  
209 Google (Abadi et al., 2016; <https://www.tensorflow.org/>). By employing an array of  
210 varied network architectures, we capitalize on the unique strengths of each structure to  
211 synthesize a more accurate and reliable estimation of PBLH. Figure 1 outlines the  
212 DNN's comprehensive design, beginning with the input layer that ingests a suite of  
213 morning meteorological features. The DNN model derives the PBLH from surface  
214 meteorological parameters. We also incorporate boundary layer heights derived from  
215 sensible heat and parcel methods ( $BLH_{parcel}$  and  $BLH_{SH}$ ) as inputs. Specifically,  
216  $BLH_{parcel}$  is calculated based on the morning profile of potential temperature  
217 (Holzworth. 1964), while  $BLH_{SH}$  is determined using the surface temperature

218 combined with surface sensible heat, following the methodologies (Stull, 1988; Su et  
219 al. 2023). We first present a preliminary run for the model to obtain the importance of  
220 each input feature. Then, these inputs undergo a filtration process based on their  
221 importance (Date and Kikuchi, 2018; Altmann et al. 2010), ensuring that only the  
222 impactful data guide the model (detailed in Section 3.3). Subsequently, the filtered  
223 inputs traverse through an ensemble of ten structures with distinct hidden layers. Each  
224 structure here represents an ensemble member and contributes to the prediction of  
225 PBLH in its unique way (Ganaie et al. 2022). The ensemble employs a three-layer base  
226 structure [52, 28, 16] for neural networks, from which ten unique configurations are  
227 derived by applying random perturbations to the default settings of the base structure.  
228 These different structures for ensembles 1-10 are presented in Table 1.

229 At the final stage, the model use the PBLH esimations from different ensembles to  
230 get a mean value as the final PBLH retrieval. This process allows the model to leverage  
231 the different results of all structures and enhance the generalizability of results. In the  
232 DNN model, neuron biases in the output and hidden layers are important for the  
233 network's architecture (Battaglia et al. 2018). These biases serve as fine-tuning  
234 parameters to adjust the activation thresholds of neurons in different layers and further  
235 refine the model's predictive capabilities. Neuron biases are initialized with small  
236 random values at the start of the training process and then iteratively adjusted according  
237 to the network weights during the training. Normalization is a preprocessing technique  
238 that often leads to improvements in model training by scaling the input features and  
239 target values to a standard range (Raju et al. 2020). The normalization process was

240 applied to each input data to ensure that they have a zero mean and a standard deviation  
241 of one, as well as the target data. This standardization scales the different input data to  
242 a similar range, and thus, contributes a more stable and efficient training process.

243 The hidden layers of the DNN model incorporate L2 regularization to curtail  
244 overfitting, while batch normalization aids in stabilizing learning. Moreover, a dropout  
245 rate of 0.2 helps the model to generalize better by reducing reliance on any specific  
246 neurons during training. We choose the Adam optimizer and mean squared error as the  
247 loss function, which aligns with one of the best practices for regression models (Zhang.  
248 2018). The mean absolute error is selected as a metric to evaluate the model's accuracy  
249 during the training. We incorporate the early stopping and learning rate reduction  
250 callbacks in in the model's training for regularization and fine-tuning (Liu et al. 2019).  
251 Such measures ensure optimal performance by terminating training at the right juncture  
252 and avoid the overfitting in the final results.

253

### 254 **3.2 Training the DNN Model**

255 The training of the DNN model was conducted using a PBLH dataset enriched by  
256 SONDE and lidar measurements during 1994 to 2016 over the SGP. Table 2 presents  
257 the distribution of dataset samples under different local time, which were important for  
258 both the training and validation processes of the DNN model. The primary dataset (i.e.,  
259 PBLH derived from SONDE measurements) is listed in the first column and are  
260 available routinely for 5, 11, and 17 LT. The training dataset was augmented with the  
261 combined MPL-SONDE PBLH dataset (Su et al. 2020b) and the Doppler Lidar-derived

262 PBLH (Sivaraman and Zhang, 2021) to address the gaps where SONDE measurements  
263 were not available. In instances where radiosonde data are unavailable, the lidar datasets  
264 are used for training, contingent upon their agreement with radiosonde measurements  
265 within a margin of 0.2 km over a 3-hour window. Specifically, out of the total  
266 comparisons during the study period, 40.2% of the lidar measurements do not agree  
267 within the 0.2 km threshold with the SONDE results. The cases with relatively larger  
268 inconsistencies stem from various factors, including instrumental errors, rainy  
269 conditions, stable PBL conditions, differing definitions, and lidar signal attenuation, as  
270 discussed in previous studies (Su et al., 2020b; Kotthaus et al., 2023). These cases were  
271 excluded from the DNN model training to maintain the quality of the process.

272 For the purpose of training the DNN model, 70% of the hourly data from both  
273 SONDE and the lidar combined dataset were randomly selected. The remaining 30%  
274 dataset, comprises the portion of SONDE measurements set aside for validation  
275 purposes, including a separate subset from the years 2017 to 2020 to test the model's  
276 predictive capabilities on independent data. This training and validation scheme ensures  
277 that the DNN model is not only well-trained but also thoroughly evaluated, reinforcing  
278 its reliability in accurately estimating PBLH. As morning SONDE data constitute the  
279 primary input and boundary conditions for the model, the validation of PBLH retrievals  
280 is consequently confined to the 08:00 to 18:00 LT.

281

282

Formatted: Normal (Web), Justified, Indent: First line: 0.2",  
Pattern: Clear (White)

### 283 3.3 Feature Importance Score

284 In the DNN model, we quantified the significance of each input parameter using the  
 285 permutation importance technique, which is a widely-used method for the deep learning  
 286 (Date and Kikuchi, 2018; Altmann et al. 2010; Breiman, L., 2001). Initially, we carry  
 287 out a test run to determine a baseline performance by calculating the mean absolute  
 288 error (MAE) on the validation set. Then, each feature within this set was then  
 289 individually shuffled, severing its correlation with the target PBLH, and the MAE was  
 290 recalculated. Compared to the baseline performance, the increase in MAE from this  
 291 shuffled state indicates the feature's predictive value: the greater the increase, the more  
 292 significant the feature. We repeat this shuffling and evaluation for 15 times, each with  
 293 a unique random seed to ensure statistical robustness. Furthermore, we calculated the  
 294 average MAE increase across these iterations as the importance score. These scores are  
 295 expressed as percentages, with each feature's importance score normalized to sum to  
 296 100%. Each score quantitatively represents how much the shuffling of a feature  
 297 increases the MAE, indicating the relative significance of that feature in the model's  
 298 predictive accuracy and facilitating a straightforward comparison of the influence of  
 299 each feature within the model. Therefore, we derived a composite importance metric  
 300 for feature groups to represent their significance as the cumulative sum of related inputs.

301 Figure 2 presents the importance scores to demonstrate the relative influence of  
 302 different feature groups on the model's performance. Prominently, features such as the  
 303  $BLH_{parcel}$ , morning potential temperature profiles ( $\theta_{profile}$ ), and surface relative  
 304 humidity are identified as pivotal most important three features, with their substantial

305 impact on the accuracy of PBLH estimation being highlighted.  $BLH_{parcel}$  is defined as  
306 the height where the morning potential temperature first exceeds the current surface  
307 potential temperature by more than 1.5 K (Holzworth, 1964; Chu et al., 2019). Among  
308 these features,  $BLH_{parcel}$  captures the response of the PBL to surface heating, which  
309 can drastically affect local convection and thus serves as one of the key parameters in  
310 the DNN model. Incorporating this parameter and its association with PBL  
311 development better simulates diurnal variations of PBLH in the DNN model.  
312 Meanwhile, the morning  $\theta$  profile represents the vertical stratification of  
313 thermodynamics and is essential for understanding stability and mixing processes  
314 within the PBL. Thus,  $\theta$  profile serves as the initial boundary condition for the PBLH  
315 estimation with a significant importance score. Surface relative humidity also emerges  
316 as a key influencer, affecting the model's performance significantly. Humidity levels  
317 influence the condensation and evaporation processes within the PBL, which are  
318 important in determining its vertical extent layer and structure. Fair-weather and dry  
319 conditions are typically associated with a more turbulent and higher PBL. Conversely,  
320 high surface humidity often contributes to the formation of boundary layer clouds,  
321 which introduces complex interactions with PBL thermodynamics.

322 In this analysis, each feature, such as  $\theta$  profile, comprises several different inputs,  
323 and the relative importance scores presented in Figure 2 are calculated as the cumulative  
324 sum of these inputs. Complementing this, Table 3 offers an exhaustive breakdown of  
325 importance scores for all considered input features within the deep learning model. In  
326 refining the model, features contributing a negligible or negative effect on performance

327 (i.e., importance scores less than zero) are excluded. As a result, this selection criterion  
328 has led to the inclusion of 58 out of the original 64 features. This process ensures we  
329 only use inputs with a proven positive influence in the DNN model.

330

## 331 **4 Evaluation of Deep Learning Model**

### 332 **4.1 Comparative analysis of biases among different datasets**

333 A critical component of evaluating our deep learning model's efficacy is analyzing  
334 the biases of individual ensemble members and their collective output. Figure 3 offers  
335 a visual assessment of the mean absolute error (MAE), root mean square error (RMSE),  
336 and correlation coefficient (R) for each ensemble member, alongside a comparison with  
337 the ensemble mean (average of all individual ensemble members). The plotted data  
338 points reveal the variation in performance across different model architectures, while  
339 the ensemble mean, represented by the horizontal dashed lines, indicates the collective  
340 accuracy of the ensemble approach. The structures of different hidden layer  
341 configurations are listed in the Table 1.

342 This methodological consolidation results in a more reliable and accurate PBLH  
343 estimation, leveraging the strengths and mitigating the weaknesses of individual  
344 models. By integrating multiple neural network configurations, we revealed that an  
345 ensemble prediction that consistently outperforms the individual models. This strategy  
346 can improve the MAE by up to 4.4%, rendering the model less dependent on any  
347 specific structural configuration.



348 An in-depth comparative analysis of biases among various PBLH estimation  
349 methods is essential for validating the reliability and accuracy of the DNN developed  
350 in this study. Figure 4 illustrates the MAE trends for several methods over a multi-year  
351 span, with the SONDE-derived PBLH serving as the benchmark for ground truth. The  
352 analysis reveals the performance of different methodologies: the DNN approach,  
353 doppler lidar, ceilometer, MPL, and Raman lidar. Significantly, the DNN model,  
354 depicted in black, maintains a consistent MAE trend throughout the trained period  
355 (1994-2016) as well as the subsequent untrained period (2017-2020), demonstrating  
356 robust predictive stability. In contrast, the remote sensing-based methods show a  
357 reduction in bias from 2010 to 2022, possibly due to the improvement of remote sensing  
358 data quality. The discrepancy in PBLH estimates between the DNN and SONDE  
359 remains consistently lower than those observed with conventional remote sensing  
360 techniques.

361 Figure 5 provides a detailed evaluation of the DNN model in comparison to  
362 ceilometer and doppler lidar-derived PBLH, as these two methods have demonstrated  
363 the high quality with more than nine years of datasets. Figure 5a-b contrast the PBLH  
364 predictions from the DNN model for both the trained period (1994-2016) and untrained  
365 periods (2017-2020), respectively, showcasing strong correlations and low MAEs,  
366 indicative of the model's robust training and generalization capabilities. Figure 5c-d  
367 further this examination with ceilometer and Doppler lidar comparisons, respectively.  
368 Overall, Doppler lidar exhibits a closer alignment with SONDE-derived PBLH than the  
369 ceilometer. However, the MAE from Doppler lidar-based estimates is still

370 approximately 48% higher than those derived from the DNN model. The correlation  
371 coefficient for the DNN-derived PBLH estimates has seen a substantial improvement,  
372 rising from the 0.5-0.6 range typically observed with remote sensing-based PBLH  
373 methods to exceed 0.8 when compared to SONDE-derived PBLH measurements. This  
374 comparative analysis not only confirms the DNN model's accuracy but also offers  
375 insights into the relative performance of various contemporary PBLH estimation  
376 methodologies.

377

#### 378 **4.2 Performances of PBLH retrievals under different conditions**

379 The performance of PBLH retrievals under varying atmospheric conditions is a  
380 crucial aspect of model evaluation. In Figure 6, the seasonal diurnal cycles of PBLH  
381 estimated by different methods are presented, offering information into the diurnal and  
382 seasonal evolution of PBL. As PBLH demonstrates notable variations for different  
383 seasons and local time with large differences between summer and winter, the DNN  
384 and Doppler lidar estimates show good agreement and closely track the variations  
385 observed in SONDE data. Meanwhile, the ceilometer presents an underestimation of  
386 PBLH, especially for the summer afternoon, indicating the potential bias of ceilometer  
387 derived PBLH under a convective environment.

388 Figure 7 illustrates the diurnal variation in the model's performance by comparing  
389 the correlation coefficient, RMSE, and MAE against SONDE-derived PBLH as the  
390 reference. The bar graphs for each local time hour offer a comparison of the RMSE and  
391 MAE, as well as the correlation, showcasing the model's precision and consistency

392 relative to remote sensing methods (i.e., ceilometer and Doppler lidar). The ceilometer-  
393 derived PBLH exhibits the greatest variations during different hours, particularly  
394 around noon, suggesting a time-dependent bias in its measurements. Conversely, both  
395 the DNN and Doppler lidar-derived PBLH demonstrate stable performance in term of  
396 MAE and RMSE throughout the day. Regarding the correlation, remote sensing  
397 methods like ceilometer and Doppler lidar exhibit a lower correlation with SONDE-  
398 derived PBLH, especially in the early hours (8-9 LT) with a value of 0.1-0.3, indicating  
399 potential limitations in their reliability during these times. On the other hand, the DNN  
400 model shows a relatively good correlation with SONDE retrievals (above 0.6 under  
401 different hours). This comparison shows the efficacy of DNN in tracking the diurnal  
402 cycle of PBLH.

403 Continuing our assessment of the DNN model, we analyze the DNN model's  
404 monthly performance in estimating PBLH, as shown in Figure 8. The analysis compares  
405 MAE, RMSE, and correlation coefficients for each month to assess the model's  
406 precision and dependability. The summer months (June-July-August) exhibit higher  
407 biases, with MAE values for the DNN, ceilometer, and Doppler lidar at 0.3 km, 0.56  
408 km, and 0.45 km, respectively. In contrast, the winter months (December-January-  
409 February) show reduced biases, with MAE values of 0.2 km for the DNN, 0.27 km for  
410 the ceilometer, and 0.24 km for the Doppler lidar. Specifically, the DNN model shows  
411 a much lower bias during the summer season. Compared to the remote sensing-based  
412 retrievals, the DNN-derived PBLH shows a much better agreement with SONDE-

413 derived PBLH, increasing from 0.3-0.6 to approximately 0.8 in term of correlation  
414 coefficients.

415 Figure 9 presents the biases of PBLH retrievals under clear-sky and low cloud  
416 conditions. We calculated biases as the absolute deviation from the mean PBLH for  
417 each condition, focusing particularly on the differences between low cloud (maximum  
418 cloud fraction between 0-4 km exceeding 1%) and clear-sky (total cloud fraction below  
419 1%) scenarios. [The threshold of 1% for cloud fraction is also used to identify cloud base  
420 height \(CBH\) in the European Centre for Medium-Range Weather Forecasts' fifth-  
421 generation global reanalysis \(ERA-5, Hersbach et al., 2023\).](#) The violin plots in this  
422 figure illustrate the data distribution of biases for each method to demonstrate their  
423 variability. For the DNN model and ceilometer, the relative biases between clear and  
424 cloudy conditions are comparable and the difference is less than than 1%. This suggests  
425 a consistent performance across these atmospheric states. However, the Doppler lidar  
426 exhibits a larger disparity, showing a 5.5% bias under cloudy conditions compared to  
427 clear skies. Moreover, the spread of biases (shaded areas and error bars) is notably wider  
428 for both the ceilometer and Doppler lidar. This indicates large variability in their  
429 performance. For all three methods, the mean biases are notably higher than the median  
430 values. Such differences indicate that the mean values are notably influenced by outliers  
431 under both clear-sky and cloudy conditions.

432 [The evolution of the PBLH under shallow cumulus conditions offers insights into  
433 the interactions between clouds, PBL, and land surface \(Zhang and Klein, 2010, 2013\).](#)  
434 [Figure 10 demonstrates the variations of PBLH measurements from different methods](#)

435 during conditions typical of shallow cumulus clouds. Shallow cumulus clouds were  
436 identified following Su et al. (2024b). Specifically, these coupled clouds form post-  
437 sunrise; and the sky must not be overcast, characterized by a cloud fraction less than  
438 90%. This selection criterion ensures that the observed cloud formations are primarily  
439 driven by surface heating and local convection. The DNN model closely matches the  
440 SONDE-derived PBLH and the CBH from ARSCL. This alignment underscores the  
441 physical validity of the DNN approach, confirming its capability to replicate traditional  
442 measurement techniques to a good extend of accuracy accurately. Meanwhile, Doppler  
443 lidar-derived PBLH retrievals also show high consistency with SONDE measurements,  
444 whereas ceilometer-derived PBLH generally underestimates values under shallow  
445 cumulus conditions.

446 Figure 10 also demonstrates the general relationship between the development of  
447 shallow cumulus clouds and the PBL, which are driven by local convection and  
448 turbulence. The formation of these cumulus clouds is linked to rising thermals and an  
449 increase in surface heat fluxes, essential for driving vertical mixing within the sub-cloud  
450 layer. This relationship is evidenced by the increased occurrence of cumulus clouds  
451 along with an increase in DNN-derived PBLH from morning to late afternoon.  
452 Specifically, during periods with a high frequency of shallow cumulus, the DNN-  
453 derived PBLH often surpasses the CBH. This indicates that rising air parcels extend  
454 beyond the condensation level, facilitating the formation and development of coupled  
455 cumulus clouds.

456 In this context, these analyses confirm the physical consistency of DNN-derived  
457 PBLH with traditional measurement techniques and highlight its physically reasonable  
458 variations during cloudy conditions. The results presented in this section

459 ~~The analyses presented in this section~~ illustrate the effectiveness of the DNN model  
460 in capturing the PBLH variations across different local times, seasons, and ~~atmospheric~~  
461 ~~cloudy~~ conditions. Compared to the traditional remote sensing methods, the DNN  
462 model exhibits relatively good accuracy in aligning with SONDE-derived PBLH,  
463 indicating its capability and stable performance under different scenarios.

464

#### 465 **4.3 Testing the DNN Model's Adaptability**

466 The DNN model relies on the incorporation of morning temperature profiles as  
467 inputs, such as detailed in Table 3. This dependency prompts the question of how to  
468 proceed the DNN model in the absence of SONDE data at specific locations. As a  
469 solution, we suggest employing morning temperature profiles from the ~~European~~  
470 ~~Centre for Medium Range Weather Forecasts' fifth-generation global reanalysis (ERA-~~  
471 ~~5; (Hersbach et al., 2020) dataset when radiosonde data is not available to maintain the~~  
472 ~~model's operational integrity under for the conditions without SONDE data sounding-~~  
473 ~~data-constrained conditions~~. As one of the most advanced reanalysis data, the ERA-5  
474 is generated by the Integrated Forecasting System coupled with a data assimilation  
475 system, and offer the meteorological data at a spatial resolution of 0.25°- 0.25°.

476 Figure 11 assess the performance of DNN produced by multi-sources field  
477 observations in estimating the PBLH by using morning temperature profiles from ERA-

478 5 (5 LT) and observed surface meteorological data. The temperature profiles in ERA-5  
479 have a vertical resolution of 25-hPa in the lower atmosphere and are interpolated into  
480 different levels described in Table 3. By utilizing ERA-5 morning profiles, the model  
481 demonstrates similar performance to those results achieved with radiosonde inputs, as  
482 evidenced by comparing Figure ~~10a-11a~~ and Figure 5. Moreover, this alternative  
483 approach also shows enhanced accuracy over the native PBLH model outputs from  
484 ERA-5, increasing the correlation coefficient from 0.74 to 0.86 and reducing the MAE  
485 from 0.3 km to 0.25 km. In addition, it is important to acknowledge that the PBLH  
486 represented in ERA-5 is indicative of a grid-average value, approximately 25 km in  
487 scale, and therefore inherently differs from site-specific data.

488 These findings highlight the alternative DNN model's robustness, offering a reliable  
489 substitute for radiosonde data by leveraging reanalysis data with similar performance.  
490 This demonstrates the DNN model's adaptability and potential as a practical tool for  
491 PBLH estimation across various meteorological sites, especially in regions or periods  
492 where radiosonde data may be lacking.

493 We further test the adaptability and generalizability of the DNN model, by applying  
494 across different climatic and geographic regions. To this end, we extended our model  
495 evaluation to include SONDE and surface meteorological data from the GoAmazon  
496 (Tropical Rainforest) and CACTI (Middle Latitude Mountain) field campaigns.  
497 Seasonality is accounted for as an input variable in the DNN model, with months in the  
498 Southern Hemisphere adjusted to reflect their Northern Hemisphere seasonal  
499 counterparts (e.g., July inputs are treated as January). The normalization process

500 (Section 3.1) was reapplied for the CACTI campaign data to adjust for notable pressure  
501 level variations, ensuring input standardization with zero mean and unit variance.

502 Figure 12+ presents the model's performance, in comparison to SONDE  
503 observations for both GoAmazon and CACTI campaigns. The DNN model  
504 demonstrates commendable adaptability, maintaining a strong correlation (0.86-0.88)  
505 with SONDE measurements (Figure 11+12a-b). Further comparison is provided, which  
506 assess the performance of ceilometer derived PBLH against SONDE for the same  
507 campaigns. When assessing the performance of the ceilometer-derived PBLH against  
508 SONDE for the same campaigns, the DNN model exhibited both stronger correlations  
509 and smaller biases, as shown in Figure 12+b-d.

510 Nevertheless, the analysis highlighted the presence of systematic biases, with  
511 relatively larger MAE at the GoAmazon and CACTI sites compared to the SGP site.  
512 Figure 13+ underscores this by presenting a comparative analysis of PBLH means and  
513 standard deviations across the three ARM sites. The early morning measurements  
514 during 05-07 LT are excluded. The results, derived from SONDE, the DNN model,  
515 ceilometer, and Doppler lidar data, reveal average differences in PBLH means relative  
516 to SONDE. These differences suggest an overestimation (+15%) and underestimation  
517 (-23%) by the DNN model for the GoAmazon and CACTI sites, respectively, compared  
518 to the more consistent PBLH values at the SGP site.

519 The evident systematic deviations when applying the SGP-trained DNN model to  
520 the diverse environments of GoAmazon and CACTI underscore the challenges in  
521 generalizing the model to regions with significantly different meteorological



522 backgrounds. These findings point to the potential of DNN models for PBLH estimation  
523 while also highlighting the necessity for region-specific model adjustments.

524

## 525 **5 Summary**

526 This study has developed a Multi-Structure DNN model for estimating PBLH using  
527 conventional meteorological data. The DNN model is developed by leveraging a long-  
528 term dataset of PBLH derived from radiosonde data and augmented with high-  
529 resolution MPL and Doppler lidar observations. This model produced an PBLH dataset  
530 over the SGP with robust accuracy, consistently yielding lower bias values across  
531 various conditions and datasets. Utilizing conventional meteorological data, this  
532 method generates a 27-year dataset over the SGP, encompassing periods with limited  
533 remote sensing data availability. In situations where morning radiosonde data is  
534 unavailable, ERA-5 data can be effectively employed to initiate the model, offering a  
535 practical alternative.

536 An important aspect of this research involved comparing DNN models with diverse  
537 remote sensing instruments. Although these instruments offer high temporal and  
538 vertical resolution, discrepancies in PBLH estimation remain. Our DNN model,  
539 leveraging a broad range of input features refined by their importance, constructs a  
540 representation of PBL evolutions, frequently demonstrating a closer agreement with  
541 SONDE-derived PBLH. In the absence of remote sensing data, the DNN model can  
542 produce high-quality PBLH results from the conventional meteorology data.

543 The study has shown the DNN model's ability to synthesize complex patterns from  
544 meteorological data, reflecting the versatility of machine learning in simulating the  
545 boundary layer processes. Its application to varied geographic terrains and climates  
546 during the GoAmazon and CACTI campaigns has further validated its adaptability,  
547 demonstrating a high correlation between DNN-derived PBLH and SONDE-derived  
548 PBLH. Nonetheless, systematic biases in regions outside the SGP highlight the  
549 influence of regional factors in PBLH estimation and suggest the need for region-  
550 specific refinements to the model.

551 In summary, this research introduces a machine learning framework for PBLH  
552 estimation that is able to generate high-quality PBLH using meteorological data,  
553 independent of remote sensing instruments. This methodology, alongside the datasets  
554 derived from the deep learning model, is beneficial in advancing our understanding of  
555 PBL daytime development including thermodynamics and dynamics. It also has  
556 implications for improved representation of the PBL processes in weather forecasting  
557 and climate models, particularly by offering the potential to diagnose PBL in models  
558 through the integration of modeled meteorological data as input. Future efforts will be  
559 directed towards refining this model to ensure its wide applicability over a global scale.  
560 These developments aim to effectively tackle the challenges of systematic biases and  
561 regional variability in PBLH estimation.

562

563 **Data Availability.** ARM radiosonde data, surface fluxes, and cloud masks are available  
564 at <https://doi.org/10.5439/1333748> (ARM User Facility, 1994). The datasets of

565 planetary boundary layer height used in this study can be downloaded from  
566 [https://adc.arm.gov/discovery/#/results/instrument\\_class\\_code::pblht](https://adc.arm.gov/discovery/#/results/instrument_class_code::pblht) (last access: 7  
567 January 2024; ARM User Facility, 2024). Climate Data Store offers the ERA-5  
568 reanalysis data (<https://doi.org/10.24381/cds.adbb2d47>, Hersbach et al., 2023). The  
569 DNN-derived PBLH datasets over the SGP, CACTI, and GoAmazon are available at  
570 Zenodo (<https://zenodo.org/records/10633811>, Su, 2024) and will be uploaded to ARM  
571 data archive as a product with detailed information upon acceptance.

572

573 **Author contributions.** TS conceptualized this study and carried out the analysis. TS  
574 and YZ interpreted the data and wrote the manuscript. YZ supervised the project.

575

576 **Competing interests.** The contact author has declared that neither they nor their co-  
577 authors have any competing interests.

578

579 **Acknowledgements:** We acknowledge the provision of radiosonde, lidar data, surface  
580 meteorological data, and cloud products by the U.S. Department of Energy's ARM  
581 program. Work at LLNL is performed under the auspices of the U.S. DOE by Lawrence  
582 Livermore National Laboratory under Contract DE-AC52-07NA27344. This research  
583 used resources of the National Energy Research Scientific Computing Center  
584 (NERSC), a U.S. Department of Energy Office of Science User Facility located at  
585 Lawrence Berkeley National Laboratory, operated under Contract No. DE-AC02-  
586 05CH11231.

587

588 **Financial support.** This work is supported by the DOE [Office of Science](#) Atmospheric  
589 System Research (ASR) [program](#) Science Focus Area (SFA) [THREAD](#)-project, [Tying](#)  
590 [in High Resolution E3SM with ARM Data \(THREAD\)](#).

591

## 592 **References**

593

594

595 Abadi, M., Agarwal, A., Barham, P., Brevdo, E., Chen, Z., Citro, C., Corrado, G.S.,  
596 Davis, A., Dean, J., Devin, M. and Ghemawat, S., 2016. Tensorflow: Large-scale  
597 machine learning on heterogeneous distributed systems. arXiv preprint  
598 arXiv:1603.04467.

599 Altmann, A., Tološi, L., Sander, O. and Lengauer, T., 2010. Permutation importance:  
600 a corrected feature importance measure. *Bioinformatics*, 26(10), pp.1340-1347.

601 [ARM User Facility. \(1994\). ARM best estimate data products \(ARMBEATM\).  
602 Southern Great Plains \(SGP\) central facility, Lamont, OK \(C1\). Compiled by C.  
603 Xiao and X. Shaocheng \[Dataset\]. ARM Data Center.  
604 <https://doi.org/10.5439/1333748>](#)

605 ARM User Facility. (2024). PLANETARY BOUNDARY LAYER HEIGHT.  
606 Southern Great Plains (SGP) central facility, Lamont, OK (C1). [Dataset]. ARM  
607 Data Center. [https://adc.arm.gov/discovery/#/results/instrument\\_class\\_code::pblht](https://adc.arm.gov/discovery/#/results/instrument_class_code::pblht)  
608 (last access: 7 January 2024)

609 Atmospheric Radiation Measurement (ARM) user facility. 2015. Planetary Boundary  
610 Layer Height (PBLHTSONDE1MCFARL). 2024-04-16 to 2024-04-19, ARM  
611 Mobile Facility (ACX) Off the Coast of California - NOAA Ship Ronald H.  
612 Brown; AMF2 (M1). Compiled by D. Zhang and D. Zhang. ARM Data Center.  
613 Data set accessed 2024-03-05 at <http://dx.doi.org/10.5439/1991783>.

614 Barlow, J.F., Dunbar, T.M., Nemitz, E.G., Wood, C.R., Gallagher, M.W., Davies, F.,  
615 O'Connor, E. and Harrison, R.M., 2011. Boundary layer dynamics over London,  
616 UK, as observed using Doppler lidar during REPARTEE-II. *Atmospheric  
617 Chemistry and Physics*, 11(5), pp.2111-2125.

618 Battaglia, P.W., Hamrick, J.B., Bapst, V., Sanchez-Gonzalez, A., Zambaldi, V.,  
619 Malinowski, M., Tacchetti, A., Raposo, D., Santoro, A., Faulkner, R. and  
620 Gulcehre, C., 2018. Relational inductive biases, deep learning, and graph  
621 networks. arXiv preprint arXiv:1806.01261.

622 Beamesderfer, E.R., Buechner, C., Faiola, C., Helbig, M., Sanchez-Mejia, Z.M.,  
623 Yáñez-Serrano, A.M., Zhang, Y. and Richardson, A.D., 2022. Advancing cross-

**Formatted:** Heading 1, Indent: Left: 0", First line: 0",  
Automatically adjust right indent when grid is defined, Adjust  
space between Latin and Asian text, Adjust space between  
Asian text and numbers

624 disciplinary understanding of land-atmosphere interactions. *Journal of*  
625 *Geophysical Research: Biogeosciences*, 127(2), p.e2021JG006707.

626 [Bianco, L., and J. M. Wilczak, 2002: Convective boundary layer depth: Improved](#)  
627 [measurements by Doppler radar wind profiler using fuzzy logic methods. \*J.\*](#)  
628 [Atmos. Oceanic Technol.](#), 19, 1745–1758, <https://doi.org/10.1175/1520->  
629 [0426\(2002\)019,1745: CBLDIM.2.0.CO:2.](#)

630 [Bianco, L., Wilczak, J. M., & White, A. B. \(2008\). Convective boundary layer depth](#)  
631 [estimation from wind profilers: Statistical comparison between an automated](#)  
632 [algorithm and expert estimations. \*Journal of Atmospheric and Oceanic\*](#)  
633 [Technology](#), 25(8), 1397-1413.

634 Breiman, L., 2001: Random forests. *Mach. Learn.*, 45, 5–32,  
635 <https://doi.org/10.1023/A:1010933404324>.

636 Cadeddu, M. P., Turner, D. D., and Liljegren, J. C., 2009. A neural network for real-  
637 time retrievals of PWV and LWP from Arctic millimeter-wave ground-based  
638 observations, *IEEE T. Geosci. Remote*, 47, 1887–1900.

639 Caughey, S.J. (1984). Observed characteristics of the atmospheric boundary layer. In  
640 *Atmospheric turbulence and air pollution modelling* (pp. 107-158). Springer,  
641 Dordrecht.

642 Chu, Y., Li, J., Li, C., Tan, W., Su, T. and Li, J. (2019). Seasonal and diurnal  
643 variability of planetary boundary layer height in Beijing: Intercomparison between  
644 MPL and WRF results. *Atmospheric research*, 227, pp.1-13.

645 Clothiaux, E. E., Ackerman, T. P., Mace, G. G., Moran, K. P., Marchand, R. T.,  
646 Miller, M. A., and Martner, B. E. (2000): Objective determination of cloud heights  
647 and radar reflectivities using a combination of active remote sensors at the ARM  
648 CART sites. *J. Appl. Meteorol.*, 39(5), 645–665.

649 Clothiaux, E.E., Miller, M.A., Perez, R.C., Turner, D.D., Moran, K.P., Martner, B.E.,  
650 Ackerman, T.P., Mace, G.G., Marchand, R.T., Widener, K.B. and Rodriguez, D.J.  
651 (2001). The ARM millimeter wave cloud radars (MMCRs) and the active remote  
652 sensing of clouds (ARSCL) value added product (VAP) (No. DOE/SC-  
653 ARM/VAP-002.1). DOE Office of Science Atmospheric Radiation Measurement  
654 (ARM) Program (United States).

655 Cohn, S. A. and Angevine, W. M. (2000). Boundary layer height and entrainment  
656 zone thickness measured by lidars and wind-profiling radars, *J. Appl. Meteorol.*,  
657 39, 1233–1247.

658 Cook, D.R. (2018). Energy balance bowen ratio station (EBBR) instrument handbook  
659 (No. DOE/SC-ARM/TR-037). DOE Office of Science Atmospheric Radiation  
660 Measurement (ARM) Program (United States).

661 Date, Y. and Kikuchi, J., 2018. Application of a deep neural network to metabolomics  
662 studies and its performance in determining important variables. *Analytical*  
663 *chemistry*, 90(3), pp.1805-1810.

664 Davis, K.J., Gamage, N., Hagelberg, C.R., Kiemle, C., Lenschow, D.H., & Sullivan,  
665 P.P. (2000). An objective method for deriving atmospheric structure from airborne  
666 lidar observations. *Journal of Atmospheric and Oceanic Technology*, 17, 1455-  
667 1468

- 668 Deardorff, J. W. (1970). Convective velocity and temperature scales for the unstable  
669 planetary boundary layer and for Rayleigh convection. *J. atmos. Sci.*, 27(8), 1211-  
670 1213.
- 671 [Dong, X., Yu, Z., Cao, W., Shi, Y., & Ma, Q. \(2020\). A survey on ensemble learning.](#)  
672 [Frontiers of Computer Science, 14, 241-258.](#)
- 673 Emanuel, K.A. (1994). *Atmospheric convection.*: Oxford University Press on Demand
- 674 Ferrare, Richard. Raman lidar/AERI PBL Height Product. United States: N. p., 2012.  
675 Web. doi:10.5439/1169501.
- 676 Gagne II, D. J., Haupt, S. E., Nychka, D. W., and Thompson, G.: Interpretable deep  
677 learning for spatial analysis of severe hailstorms, *Mon. Weather Rev.*, 147, 2827–  
678 2845, (2019).
- 679 Ganaie, M.A., Hu, M., Malik, A.K., Tanveer, M. and Suganthan, P.N., 2022.  
680 Ensemble deep learning: A review. *Engineering Applications of Artificial*  
681 *Intelligence*, 115, p.105151.
- 682 Garratt, J. R. (1994): The atmospheric boundary layer. *Earth-Sci. Rev.*, 37(1–2), 89–  
683 134.
- 684 Guo, J., Su, T., Chen, D., Wang, J., Li, Z., Lv, Y., ... & Zhai, P. (2019). Declining  
685 summertime local-scale precipitation frequency over China and the United States,  
686 1981–2012: The disparate roles of aerosols. *Geophysical Research Letters*, 46(22),  
687 13281-13289.
- 688 Guo, J., Su, T., Li, Z., Miao, Y., Li, J., Liu, H., Xu, H., Cribb, M. and Zhai, P. (2017).  
689 Declining frequency of summertime local-scale precipitation over eastern China  
690 from 1970 to 2010 and its potential link to aerosols. *Geophysical Research*  
691 *Letters*, 44(11), pp.5700-5708.
- 692 Guo, J., Zhang, J., Shao, J., Chen, T., Bai, K., Sun, Y., Li, N., Wu, J., Li, R., Li, J. and  
693 Guo, Q., 2024. A merged continental planetary boundary layer height dataset  
694 based on high-resolution radiosonde measurements, ERA5 reanalysis, and  
695 GLDAS. *Earth System Science Data*, 16(1), pp.1-14.
- 696 Guo, J., Zhang, J., Yang, K., Liao, H., Zhang, S., Huang, K., Lv, Y., Shao, J., Yu, T.,  
697 Tong, B. and Li, J., 2021. Investigation of near-global daytime boundary layer  
698 height using high-resolution radiosondes: first results and comparison with ERA5,  
699 MERRA-2, JRA-55, and NCEP-2 reanalyses. *Atmospheric Chemistry and*  
700 *Physics*, 21(22), pp.17079-17097.
- 701 Helbig, M., Gerken, T., Beamesderfer, E.R., Baldocchi, D.D., Banerjee, T., Biraud,  
702 S.C., Brown, W.O., Brunzell, N.A., Burakowski, E.A., Burns, S.P. and  
703 Butterworth, B.J., 2021. Integrating continuous atmospheric boundary layer and  
704 tower-based flux measurements to advance understanding of land-atmosphere  
705 interactions. *Agricultural and Forest Meteorology*, 307, p.108509.
- 706 [Hersbach, H., Bell, B., Berrisford, P., Biavati, G., Horányi, A., Muñoz Sabater, J.,](#)  
707 [Nicolas, J., Peubey, C., Radu, R., Rozum, I., Schepers, D., Simmons, A., Soci, C.,](#)  
708 [Dee, D., Thépaut, J-N. \(2023\): ERA5 hourly data on single levels from 1940 to](#)  
709 [present. Copernicus Climate Change Service \(C3S\) Climate Data Store \(CDS\),](#)  
710 [DOI: https://doi.org/10.24381/cds.adbb2d47](#)

Formatted: Font: 12 pt

Formatted: Font: 12 pt

711 Hersbach, H., Bell, B., Berrisford, P., Hirahara, S., Horányi, A., Muñoz-Sabater, J.,  
712 Nicolas, J., Peubey, C., Radu, R., Schepers, D. and Simmons, A., 2020. The  
713 ERA5 global reanalysis. *Quarterly Journal of the Royal Meteorological Society*,  
714 146(730), pp.1999-2049.

715 Holdridge, D., Ritsche, M., Prell, J., and Coulter, R. (2011): Balloon-borne sounding  
716 system (SONDE) handbook, <https://www.arm.gov/capabilities/instruments/sonde>.

717 Holtslag, A.A. and Nieuwstadt, F.T. (1986). Scaling the atmospheric boundary layer.  
718 *Boundary-Layer Meteorology*, 36(1-2), pp.201-209.

719 Holzworth, G. C. (1964). Estimates of mean maximum mixing depths in the  
720 contiguous United States. *Monthly Weather Review*, 92(5), 235–242.  
721 [https://doi.org/10.1175/1520-0493\(1964\)092<0235:EOMMMD>2.3.CO;2](https://doi.org/10.1175/1520-0493(1964)092<0235:EOMMMD>2.3.CO;2)

722 Kaimal, J.C. and Finnigan, J.J. (1994). *Atmospheric boundary layer flows: their*  
723 *structure and measurement*. Oxford university press.

724 Kaimal, J.C., Wyngaard, J.C., Haugen, D.A., Coté, O.R., Izumi, Y., Caughey, S.J. and  
725 Readings, C.J., 1976. Turbulence structure in the convective boundary layer.  
726 *Journal of Atmospheric Sciences*, 33(11), pp.2152-2169.

727 Kollias, P., Bharadwaj, N., Clothiaux, E.E., Lamer, K., Oue, M., Hardin, J., Isom, B.,  
728 Lindenmaier, I., Matthews, A., Luke, E.P. and Giangrande, S.E. (2020). The ARM  
729 radar network: At the leading edge of cloud and precipitation observations.  
730 *Bulletin of the American Meteorological Society*, 101(5), pp.E588-E607.

731 Kotthaus, S., Bravo-Aranda, J.A., Collaud Coen, M., Guerrero-Rascado, J.L., Costa,  
732 M.J., Cimini, D., O'Connor, E.J., Hervo, M., Alados-Arboledas, L., Jiménez-  
733 Portaz, M. and Mona, L., 2023. Atmospheric boundary layer height from ground-  
734 based remote sensing: a review of capabilities and limitations. *Atmospheric*  
735 *Measurement Techniques*, 16(2), pp.433-479.

736 Krishnamurthy, R., Newsom, R.K., Berg, L.K., Xiao, H., Ma, P.L. and Turner, D.D.,  
737 2021. On the estimation of boundary layer heights: a machine learning approach.  
738 *Atmospheric Measurement Techniques*, 14(6), pp.4403-4424.

739 Lareau, N.P., Zhang, Y. and Klein, S.A., 2018. Observed boundary layer controls on  
740 shallow cumulus at the ARM Southern Great Plains site. *Journal of the*  
741 *Atmospheric Sciences*, 75(7), pp.2235-2255.

742 Li, H., Liu, B., Ma, X., Jin, S., Wang, W., Fan, R., Ma, Y., Wei, R. and Gong, W.,  
743 2023. Estimation of Planetary Boundary Layer Height from Lidar by Combining  
744 Gradient Method and Machine Learning Algorithms. *IEEE Transactions on*  
745 *Geoscience and Remote Sensing*.

746 Li, Z., Guo, J., Ding, A., Liao, H., Liu, J., Sun, Y., Wang, T., Xue, H., Zhang, H. and  
747 Zhu, B., 2017. Aerosol and boundary-layer interactions and impact on air quality.  
748 *National Science Review*, 4(6), pp.810-833.

749 Lilly, D.K. (1968). Models of Cloud-Topped Mixed Layers under a Strong Inversion.  
750 *Quarterly Journal of the Royal Meteorological Society*, 94, 292-&  
751 [Liu, B., Ma, Y., Guo, J., Gong, W., Zhang, Y., Mao, F., ... & Shi, Y. \(2019\).  
752 \[Boundary layer heights as derived from ground-based Radar wind profiler in  
753 \\[Beijing. IEEE Transactions on Geoscience and Remote Sensing\\]\\(#\\), 57\\(10\\), 8095-  
754 \\[8104.\\]\\(#\\)\]\(#\)](#)

755 Liu, F., Page, A., Strode, S. A., Yoshida, Y., Choi, S., Zheng, B., Lamsal, L. N., Li,  
756 C., Krotkov, N. A., Eskes, H., and Veefkind, P. (2020). Abrupt decline in  
757 tropospheric nitrogen dioxide over China after the outbreak of COVID-19.  
758 Science Advances, 6(28), eabc2992

759 Liu, L., Jiang, H., He, P., Chen, W., Liu, X., Gao, J. and Han, J., 2019. On the  
760 variance of the adaptive learning rate and beyond. arXiv preprint  
761 arXiv:1908.03265. Garratt, J.R. (1994). The atmospheric boundary layer. Earth-  
762 Science Reviews, 37(1-2), pp.89-134.

763 Liu, S. and Liang, X.Z., 2010. Observed diurnal cycle climatology of planetary  
764 boundary layer height. Journal of Climate, 23(21), pp.5790-5809.

765 Liu, Z., Chang, J., Li, H., Chen, S. and Dai, T., 2022. Estimating boundary layer  
766 height from lidar data under complex atmospheric conditions using machine  
767 learning. Remote Sensing, 14(2), p.418.

768 Mahrt, L. (1999). Stratified atmospheric boundary layers. Boundary-Layer  
769 Meteorology, 90(3), pp.375-396.

770 [Martin, S. T., Artaxo, P., Machado, L. A. T., Manzi, A. O., Souza, R. A. F. D.,](#)  
771 [Schumacher, C., ... & Wendisch, M. \(2016\). Introduction: observations and](#)  
772 [modeling of the Green Ocean Amazon \(GoAmazon2014/5\). Atmospheric](#)  
773 [Chemistry and Physics, 16\(8\), 4785-4797.](#)

774 Matsui, T., Masunaga, H., Pielke, R.A., & Tao, W.K. (2004). Impact of aerosols and  
775 atmospheric thermodynamics on cloud properties within the climate system.  
776 Geophysical Research Letters, 31

777 McGovern, A., Elmore, K. L., Gagne, D. J., Haupt, S. E., Karstens, C. D., Lagerquist,  
778 R., Smith, T., and Williams, J. K.: Using artificial intelligence to improve real-  
779 time decision-making for high-impact weather, B. Am. Meteorol. Soc., 98, 2073–  
780 2090, (2017).

781 Melfi, S.H., Spinhirne, J.D., Chou, S.H. and Palm, S.P. (1985). Lidar observations of  
782 vertically organized convection in the planetary boundary layer over the ocean.  
783 Journal of climate and applied meteorology, 24(8), pp.806-821.

784 Menut, L., Flamant, C., Pelon, J., & Flamant, P.H. (1999). Urban boundary-layer  
785 height determination from lidar measurements over the Paris area. Applied Optics,  
786 38, 945-954

787 [Mohammed, A., & Kora, R. \(2023\). A comprehensive review on ensemble deep](#)  
788 [learning: Opportunities and challenges. Journal of King Saud University-](#)  
789 [Computer and Information Sciences, 35\(2\), 757-774.](#)

790 Molero, F., Barragán, R. and Artíñano, B., 2022. Estimation of the atmospheric  
791 boundary layer height by means of machine learning techniques using ground-  
792 level meteorological data. Atmospheric Research, 279, p.106401.

793 [Molod, A., Salmun, H., and Dempsey, M., 2015: Estimating Planetary Boundary](#)  
794 [Layer Heights from NOAA Profiler Network Wind Profiler Data, J. Atmos.](#)  
795 [Ocean. Tech., 32, 1545–1561. https://doi.org/10.1175/JTECH-D-14-00155.1.](#)

796 Nielsen, M.A., 2015. Neural networks and deep learning (Vol. 25, pp. 15-24). San  
797 Francisco, CA, USA: Determination press.

Formatted: Font color: Text 1



- 798 Pang, B., Nijkamp, E. and Wu, Y.N., 2020. Deep learning with tensorflow: A review.  
799 Journal of Educational and Behavioral Statistics, 45(2), pp.227-248.
- 800 Park, O.H., Seo, S.J., & Lee, S.H. (2001). Laboratory simulation of vertical plume  
801 dispersion within a convective boundary layer - Research note. Boundary-Layer  
802 Meteorology, 99, 159-169
- 803 Raju, V.G., Lakshmi, K.P., Jain, V.M., Kalidindi, A. and Padma, V., 2020, August.  
804 Study the influence of normalization/transformation process on the accuracy of  
805 supervised classification. In 2020 Third International Conference on Smart  
806 Systems and Inventive Technology (ICSSIT) (pp. 729-735). IEEE.
- 807 Rieutord, T., Aubert, S. and Machado, T., 2021. Deriving boundary layer height from  
808 aerosol lidar using machine learning: KABL and ADABL algorithms.  
809 Atmospheric Measurement Techniques, 14(6), pp.4335-4353.
- 810 [Salmun, H., Josephs, H., & Molod, A. \(2023\). GRWP-PBLH: Global Radar Wind](#)  
811 [Profiler Planetary Boundary Layer Height Data. Bulletin of the American](#)  
812 [Meteorological Society, 104\(5\), E1044-E1057.](#)
- 813 Sawyer, V. and Li, Z., 2013. Detection, variations and intercomparison of the  
814 planetary boundary layer depth from radiosonde, lidar and infrared spectrometer.  
815 Atmospheric environment, 79, pp.518-528.
- 816 Schmidhuber, J., 2015. Deep learning in neural networks: An overview. Neural  
817 networks, 61, pp.85-117.
- 818 Seidel, D.J., Ao, C.O. and Li, K., 2010. Estimating climatological planetary boundary  
819 layer heights from radiosonde observations: Comparison of methods and  
820 uncertainty analysis. Journal of Geophysical Research: Atmospheres, 115(D16).
- 821 Sivaraman, Chitra, and Zhang, Damao. Planetary Boundary Layer Height derived  
822 from Doppler Lidar (DL) data. United States: N. p., 2021. Web.  
823 doi:10.5439/1726254.
- 824 Sleeman, J., Halem, M., Yang, Z., Caicedo, V., Demoz, B. and Delgado, R., 2020,  
825 September. A deep machine learning approach for lidar based boundary layer  
826 height detection. In IGARSS 2020-2020 IEEE international geoscience and  
827 remote sensing symposium (pp. 3676-3679). IEEE.
- 828 [Solanki, R., Guo, J., Lv, Y., Zhang, J., Wu, J., Tong, B., & Li, J. \(2022\). Elucidating](#)  
829 [the atmospheric boundary layer turbulence by combining UHF radar wind profiler](#)  
830 [and radiosonde measurements over urban area of Beijing. Urban Climate, 43,](#)  
831 [101151.](#)
- 832 Stull, R.B. (1988). An Introduction to Boundary Layer Meteorology. Dordrecht:  
833 Springer Netherlands
- 834 [Su, T. \(2024\). PBLH using DNN method \[Dataset\]. Zenodo.](#)  
835 <https://zenodo.org/records/10633811>
- 836 Su, T., Laszlo, I., Li, Z., Wei, J., & Kalluri, S. (2020a). Refining aerosol optical depth  
837 retrievals over land by constructing the relationship of spectral surface  
838 reflectances through deep learning: Application to Himawari-8. Remote Sensing  
839 of Environment, 251, 112093.

Field Code Changed

840 Su, T., Li, Z. and Zheng, Y. (2023). Cloud-Surface Coupling Alters the Morning  
841 Transition From Stable to Unstable Boundary Layer. *Geophysical Research*  
842 *Letters*, 50(5), p.e2022GL102256.

843 Su, T., Li, Z., and Kahn, R. (2020b): A new method to retrieve the diurnal variability  
844 of planetary boundary layer height from lidar under different thermodynamic  
845 stability conditions. *Remote Sens. Environ.*, 237, 111519.

846 Su, T., Li, Z., Roldán, N., Luan, Q., Yu, F.: Constraining Effects of Aerosol-Cloud  
847 Interaction by Accounting for Coupling between Cloud and Land Surface, *Science*  
848 *Advances*, 2024a (Accepted).

849 [Su, T., Li, Z., Zhang, Y., Zheng, Y., & Zhang, H.: Observation and Reanalysis](#)  
850 [Derived Relationships Between Cloud and Land Surface Fluxes Across Cumulus](#)  
851 [and Stratiform Coupling Over the Southern Great Plains. \*Geophysical Research\*](#)  
852 [Letters, 51\(8\). <https://doi.org/10.1029/2023GL108090>, 2024b.](#)

853 Su, T., Zheng, Y. and Li, Z., (2022). Methodology to determine the coupling of  
854 continental clouds with surface and boundary layer height under cloudy conditions  
855 from lidar and meteorological data. *Atmospheric Chemistry and Physics*, 22(2),  
856 pp.1453-1466.

857 Summa, D., Di Girolamo, P., Stelitano, D. and Cacciani, M., 2013. Characterization  
858 of the planetary boundary layer height and structure by Raman lidar: comparison  
859 of different approaches. *Atmospheric Measurement Techniques*, 6(12), pp.3515-  
860 3525.

861 Sze, V., Chen, Y.H., Yang, T.J. and Emer, J.S., 2017. Efficient processing of deep  
862 neural networks: A tutorial and survey. *Proceedings of the IEEE*, 105(12),  
863 pp.2295-2329.

864 Tang, S., Xie, S., Zhang, M., Tang, Q., Zhang, Y., Klein, S. A., Cook, D. R., and  
865 Sullivan, R. C. (2019): Differences in eddy-correlation and energy-balance surface  
866 turbulent heat flux measurements and their impacts on the large-scale forcing  
867 fields at the ARM SGP site. *J. Geophys. Res. Atmos.*, 124, 3301–3318,  
868 [doi.org/10.1029/2018JD029689](https://doi.org/10.1029/2018JD029689).

869 [Tao, C., Y. Zhang, Q. Tang, H. Ma, V. P. Ghate, S. Tang, S. Xie, and J. A.](#)  
870 [Santanello, 2021: Land–Atmosphere Coupling at the U.S. Southern Great Plains:](#)  
871 [A Comparison on Local Convective Regimes between ARM Observations,](#)  
872 [Reanalysis, and Climate Model Simulations. \*J. Hydrometeor.\*, 22, 463–481,](#)  
873 [https://doi.org/10.1175/JHM-D-20-0078.1.](https://doi.org/10.1175/JHM-D-20-0078.1)

874 Tucker, S.C., Brewer, W.A., Banta, R.M., Senff, C.J., Sandberg, S.P., Law, D.C.,  
875 Weickmann, A.M., & Hardesty, R.M. (2009). Doppler Lidar Estimation of Mixing  
876 Height Using Turbulence, Shear, and Aerosol Profiles. *Journal of Atmospheric*  
877 *and Oceanic Technology*, 26, 673-688

878 [Varble, A. C., Nesbitt, S. W., Salio, P., Hardin, J. C., Bharadwaj, N., Borque, P., ... &](#)  
879 [Zipser, E. J. \(2021\). Utilizing a storm-generating hotspot to study convective](#)  
880 [cloud transitions: The CACTI experiment. \*Bulletin of the American\*](#)  
881 [Meteorological Society, 102\(8\), E1597-E1620.](#)

882 Vassallo, D., Krishnamurthy, R., and Fernando, H. J. S.: Decreasing wind speed  
883 extrapolation error via domain-specific feature extraction and selection, *Wind*  
884 *Eng. Sci.*, 5, 959–975, <https://doi.org/10.5194/wes-5-959-2020>, 2020.

885 Wang, J., Su, H., Wei, C., Zheng, G., Wang, J., Su, T., Li, C., Liu, C., Pleim, J.E., Li,  
886 Z. and Ding, A., 2023. Black-carbon-induced regime transition of boundary layer  
887 development strongly amplifies severe haze. *One Earth*, 6(6), pp.751-759.

888 Wang, Y., Zheng, X., Dong, X., Xi, B., Wu, P., Logan, T., & Yung, Y. L. (2020).  
889 Impacts of long-range transport of aerosols on marine-boundary-layer clouds in  
890 the eastern North Atlantic. *Atmospheric Chemistry and Physics*, 20(23), 14741-  
891 14755.

892 Wesely, M. L., Cook, D. R., and Coulter, R. L. (1995): Surface heat flux data from  
893 energy balance Bowen ratio systems (No. ANL/ER/CP-84065; CONF-9503104-  
894 2). Argonne National Lab., IL (United States).

895 Xie, S., McCoy, R. B., Klein, S. A., Cederwall, R. T., Wiscombe, W. J., Jensen, M.  
896 P., Johnson, K. L., Clothiaux, E. E., Gaustad, K. L., Long, C. N., and Mather, J.  
897 H. (2010): Clouds and more: ARM climate modeling best estimate data: a new  
898 data product for climate studies. *Bull. Amer. Meteorol. Soc.*, 91(1), 13–20.

899 [Xue, W., Dai, X., & Liu, L. \(2020\). Remote sensing scene classification based on](#)  
900 [multi-structure deep features fusion. \*IEEE Access\*, 8, 28746-28755.](#)

901 Ye, J., Liu, L., Wang, Q., Hu, S. and Li, S., 2021. A novel machine learning algorithm  
902 for planetary boundary layer height estimation using AERI measurement data.  
903 *IEEE Geoscience and Remote Sensing Letters*, 19, pp.1-5.

904 Zhang, D., Comstock, J. and Morris, V., (2022). Comparison of planetary boundary  
905 layer height from ceilometer with ARM radiosonde data. *Atmospheric*  
906 *Measurement Techniques*, 15(16), pp.4735-4749.

907 [Zhang, Y., & Klein, S. A. \(2010\). Mechanisms affecting the transition from shallow](#)  
908 [to deep convection over land: Inferences from observations of the diurnal cycle](#)  
909 [collected at the ARM Southern Great Plains site. \*Journal of the Atmospheric\*](#)  
910 [\*Sciences\*, 67\(9\), 2943–2959. <https://doi.org/10.1175/2010jas3366.1>](#)

911 [Zhang, Y., & Klein, S. A. \(2013\). Factors controlling the vertical extent of fair-](#)  
912 [weather shallow cumulus clouds over land: Investigation of diurnal-cycle](#)  
913 [observations collected at the ARM Southern Great Plains site. \*Journal of the\*](#)  
914 [\*Atmospheric Sciences\*, 70\(4\), 1297–1315. <https://doi.org/10.1175/jas-d-12-0131.1>](#)

915 Zhang, Z., (2018), June. Improved adam optimizer for deep neural networks. In 2018  
916 IEEE/ACM 26th international symposium on quality of service (IWQoS) (pp. 1-  
917 2). IEEE.

918 **Table list:**

919 **Table 1.** This table lists the varying structures of hidden layers used by each ensemble  
920 member for PBLH estimation. Each configuration is expressed as an array, with the  
921 number of elements indicating the number of layers and each value specifying the  
922 number of neurons activated in the corresponding layer. For instance, a structure  
923 denoted as [52, 28, 16] comprises three hidden layers containing 52, 28, and 16 neurons,  
924 respectively.

925

<b>Ensemble Member</b>	<b>Different Structures in Hidden Layer</b>	<b>Ensemble Member</b>	<b>Different Structures in Hidden Layer</b>
Member 1	[52, 28, 16]	Member 6	[57, 44, 19]
Member 2	[61, 43, 20]	Member 7	[55, 43, 19]
Member 3	[59, 45, 19]	Member 8	[57, 43, 15]
Member 4	[60, 45, 23]	Member 9	[59, 41, 20, 10]
Member 5	[57, 45, 23]	Member 10	[57, 43, 18, 9]

926

927

928

929

930

931

932

933

934

935

936

937

938

939 **Table 2.** Distribution of Dataset Samples for deep learning neural network (DNN)  
 940 Training and Validation. This table details the sample data in different local time used  
 941 for the development and validation of DNN to estimate planetary boundary layer height  
 942 (PBLH). The first column lists the available PBLH derived from radiosonde (SONDE,  
 943 Liu and Liang, 2010) during various local hours from 1994 to 2016. The second column  
 944 supplements the dataset with a combined MPL and SONDE approach (Su et al. 2020b)  
 945 and Doppler Lidar-derived PBLH (Sivaraman and Zhang, 2021) used in the absence of  
 946 SONDE measurements. Seventy percent of the combined dataset from the first and  
 947 second columns was randomly selected for the model's training. The third column  
 948 provides the number of SONDE measurements available for validation purposes. Since  
 949 morning SONDE serves as the input and boundary condition.

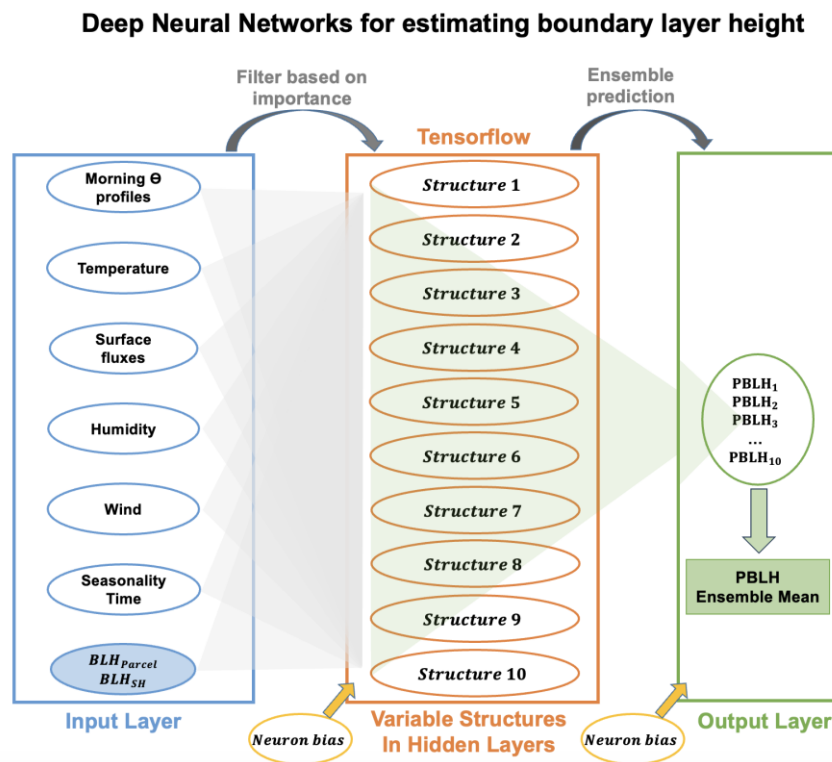
<b>Local Time (h)</b>	<b>SONDE</b>	<b>Supplement Lidar Dataset</b>	<b>SONDE for Validation</b>
5	7163	0	0
6	22	1181	0
7	3	1186	0
8	1225	2541	453
9	16	2629	8
10	9	2732	3
11	6513	13	3307
12	26	2797	9
13	14	2694	47
14	2131	2334	728
15	28	2555	9
16	3	2730	1
17	6503	2	3348

950 **Table 3. Feature Importance in the Deep Learning Model.** This table presents the The  
951 relative importance scores (%) of each input feature used in the deep learning model to  
952 estimate the planetary boundary layer height. The features include local time, month,  
953 relative humidity, U and V wind components, surface pressure, precipitation,  
954 temperature, lifting condensation level (LCL), boundary layer height derived from  
955 sensible heat and parcel methods (Sensible Heat BLH and Parcel Method BLH),  
956 sensible and latent heat, and profiles of potential temperature ( $\theta$ ) at different heights.  
957 The importance scores are expressed as percentages, indicating each feature's relative  
958 contribution to the model's predictive accuracy, normalized to sum to 100%. The  
959 importance scores quantify the relative contribution of each feature to the model's  
960 predictive accuracy.

<u>Feature</u>	<u>Importance (%)</u>	<u>Feature</u>	<u>Importance (%)</u>
<u>Local Time</u>	<u>0.385238096</u>	<u><math>\theta</math> 0.45km</u>	<u>0.589744268</u>
<u>Month</u>	<u>3.589829217</u>	<u><math>\theta</math> 0.5km</u>	<u>0.537731259</u>
<u>RH (i-1)</u>	<u>1.525447612</u>	<u><math>\theta</math> 0.55km</u>	<u>0.534610382</u>
<u>RH (i)</u>	<u>16.25123402</u>	<u><math>\theta</math> 0.6km</u>	<u>0.552997086</u>
<u>U Wind (i-1)</u>	<u>0.385834048</u>	<u><math>\theta</math> 0.65km</u>	<u>0.431060615</u>
<u>U Wind (i)</u>	<u>2.076794013</u>	<u><math>\theta</math> 0.7km</u>	<u>0.342764903</u>
<u>V Wind (i-1)</u>	<u>2.537910928</u>	<u><math>\theta</math> 0.75km</u>	<u>0.310147803</u>
<u>V Wind (i)</u>	<u>2.405275378</u>	<u><math>\theta</math> 0.8km</u>	<u>0.380120894</u>
<u>Surface Pressure (i-1)</u>	<u>0.187890954</u>	<u><math>\theta</math> 0.85km</u>	<u>0.468503984</u>
<u>Surface Pressure (i)</u>	<u>1.016443163</u>	<u><math>\theta</math> 0.9km</u>	<u>0.413498983</u>
<u>Rain Rate (i-1)</u>	<u>0.077638613</u>	<u><math>\theta</math> 0.95km</u>	<u>0.263411835</u>
<u>Rain Rate (i)</u>	<u>0.10979265</u>	<u><math>\theta</math> 1km</u>	<u>0.132168034</u>
<u>Temperature (i-1)</u>	<u>1.028603672</u>	<u><math>\theta</math> 1.1km</u>	<u>0.163035362</u>
<u>Temperature (i)</u>	<u>1.382663171</u>	<u><math>\theta</math> 1.2km</u>	<u>0.042643843</u>
<u>LCL (i-1)</u>	<u>0.330188472</u>	<u><math>\theta</math> 1.3km</u>	<u>-0.020619871</u>
<u>LCL (i)</u>	<u>2.92117154</u>	<u><math>\theta</math> 1.4km</u>	<u>-0.117425464</u>
<u>Sensible Heat BLH (i-1)</u>	<u>1.071904572</u>	<u><math>\theta</math> 1.5km</u>	<u>-0.020003889</u>
<u>Sensible Heat BLH (i)</u>	<u>2.650567178</u>	<u><math>\theta</math> 1.6km</u>	<u>0.10811159</u>
<u>Parcel Method BLH (i-1)</u>	<u>8.796298485</u>	<u><math>\theta</math> 1.7km</u>	<u>0.211953821</u>
<u>Parcel Method BLH (i)</u>	<u>22.15513884</u>	<u><math>\theta</math> 1.8km</u>	<u>0.092761568</u>
<u>Sensible Heat (i-1)</u>	<u>1.09273529</u>	<u><math>\theta</math> 1.9km</u>	<u>0.134436502</u>
<u>Sensible Heat (i)</u>	<u>0.344360459</u>	<u><math>\theta</math> 2km</u>	<u>0.109195516</u>
<u>Latent Heat (i-1)</u>	<u>1.240177933</u>	<u><math>\theta</math> 2.2km</u>	<u>-0.10805866</u>
<u>Latent Heat (i)</u>	<u>1.705848738</u>	<u><math>\theta</math> 2.4km</u>	<u>-0.217483536</u>
<u><math>\theta</math> 0.05km</u>	<u>13.55861389</u>	<u><math>\theta</math> 2.6km</u>	<u>-0.178324068</u>
<u><math>\theta</math> 0.1km</u>	<u>1.19646809</u>	<u><math>\theta</math> 2.8km</u>	<u>0.08071272</u>
<u><math>\theta</math> 0.15km</u>	<u>0.025100917</u>	<u><math>\theta</math> 3km</u>	<u>0.249503653</u>
<u><math>\theta</math> 0.2km</u>	<u>0.193888217</u>	<u><math>\theta</math> 3.2km</u>	<u>0.143137953</u>

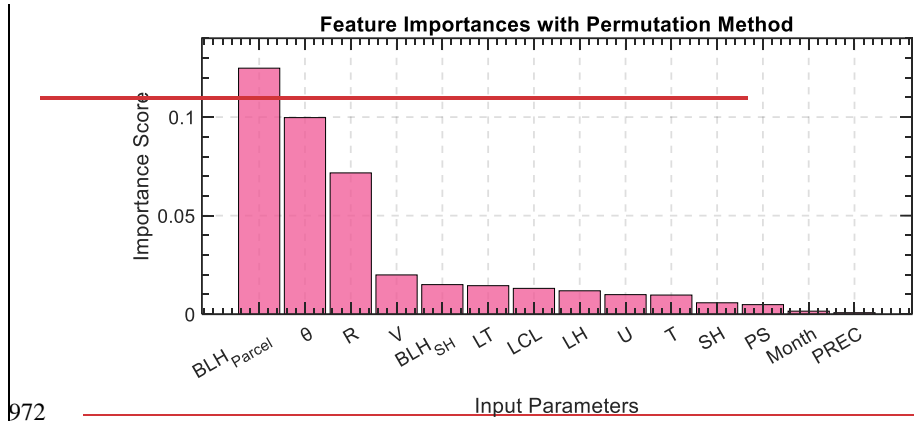
<u>0 0.25km</u>	<u>0.445161715</u>	<u>0 3.4km</u>	<u>0.19819078</u>
<u>0 0.3km</u>	<u>0.572192811</u>	<u>0 3.6km</u>	<u>0.158828504</u>
<u>0 0.35km</u>	<u>0.751498918</u>	<u>0 3.8km</u>	<u>0.185359544</u>
<u>0 0.4km</u>	<u>0.768690105</u>	<u>0 4km</u>	<u>1.046682377</u>

961 **Figures**

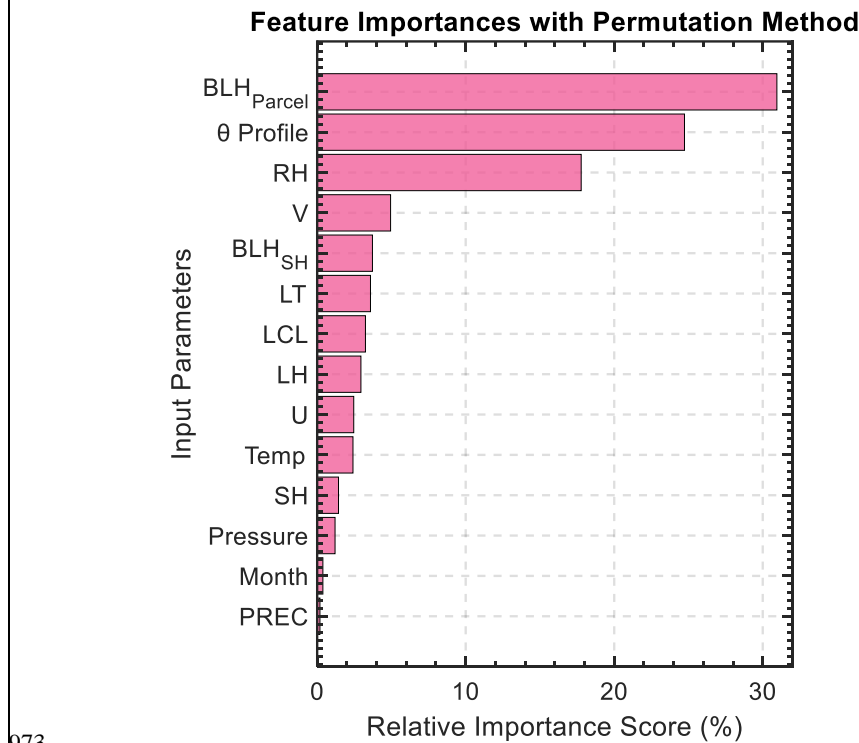


962  
963 **Figure 1.** Schematic of the multi-structure deep neural networks (DNN) used for  
964 estimating the planetary boundary layer height (PBLH). Input features, including  
965 morning potential temperature profiles, temperature, wind, humidity, surface fluxes,  
966 seasonality, and time, are filtered based on importance and fed into the network. The  
967 system comprises ten distinct hidden layer structures, each processing the inputs to  
968 model PBLH. The outputs from these structures are then synthesized to determine the  
969 final PBLH value, leveraging the diverse representations of atmospheric dynamics

970 captured by each neural network configuration. Neuron biases are applied at the output  
 971 and hidden layers to fine-tune the model's performance.



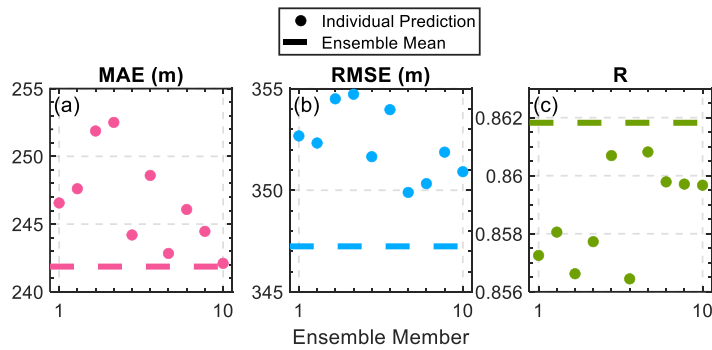
Formatted: Centered





974 **Figure 2.** Feature importance with permutation method in the deep learning model.  
 975 This table presents the importance scores of each input feature used in the deep learning  
 976 model to estimate the PBLH. The features include local time (LT), month, relative  
 977 humidity (RH), surface U and V wind components, pressure at the surface (Pressure),  
 978 precipitation (PREC), surface temperature (Temp), sensible and latent heat (SH and  
 979 LH), surface-derived lifting condensation level (LCL), boundary layer height derived  
 980 from sensible heat and parcel methods ( $BLH_{Parcel}$  and  $BLH_{SH}$ ), and morning profiles  
 981 of potential temperature ( $\theta$  Profile). The importance scores are presented as  
 982 percentages, representing each feature's relative contribution to the model's predictive  
 983 accuracy, normalized to sum to 100%. The importance scores quantify the relative  
 984 contribution of each feature to the model's predictive accuracy.

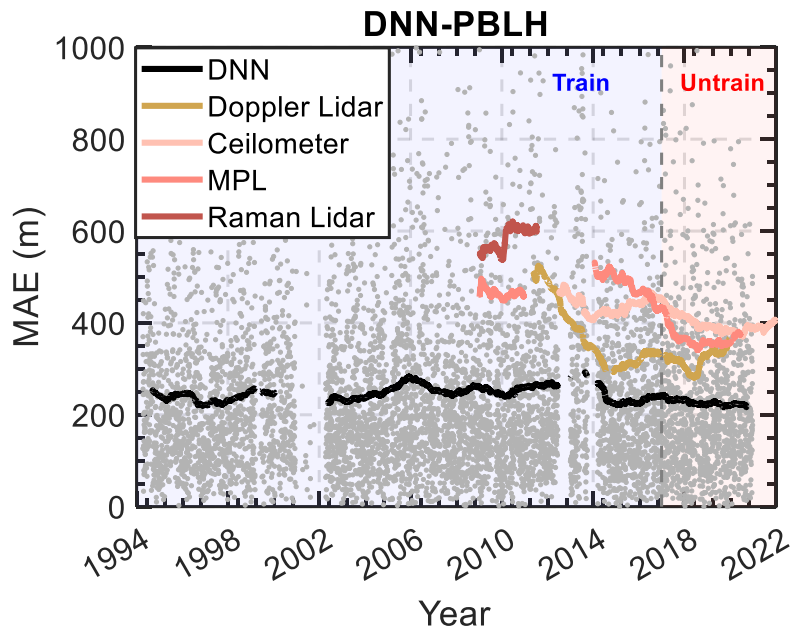
985



986

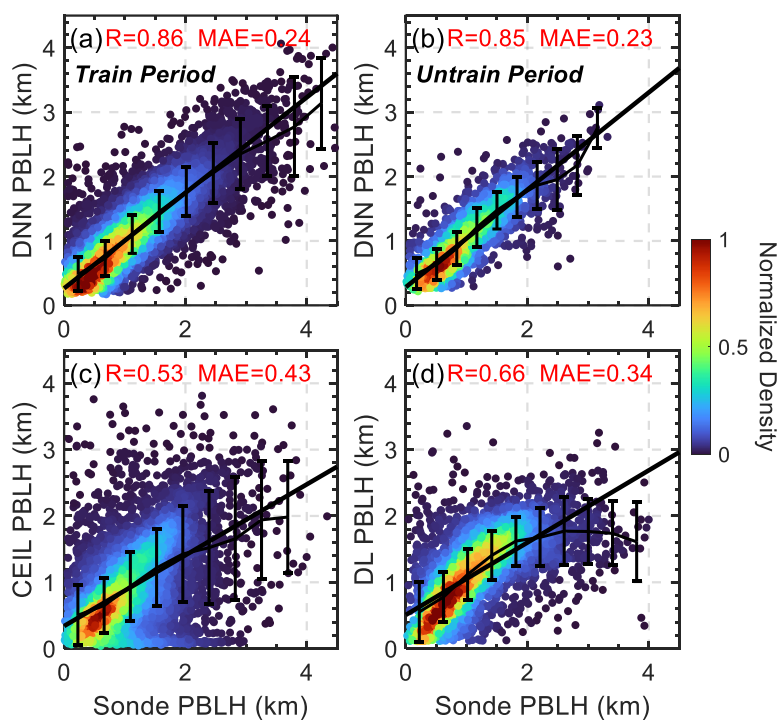
987 **Figure 3:** Performance metrics of individual ensemble members and the ensemble  
 988 mean in estimating planetary boundary layer height (PBLH). Panel (a) displays the  
 989 mean absolute error (MAE), panel (b) the root mean square error (RMSE), and panel

990 (c) the correlation coefficient (R) for each of the ten ensemble members (represented  
 991 by dots) and the ensemble mean (indicated by the horizontal dash line). The ensemble  
 992 approach demonstrates improved accuracy and reliability in PBLH estimation as  
 993 evidenced by the aggregation of individual model predictions into a robust ensemble  
 994 mean.  
 995  
 996



997  
 998 **Figure 4:** Comparative analysis of the mean absolute error (MAE) in PBLH estimation  
 999 using different methodologies. PBLH derived from SONDE is considered as the ground  
 1000 truth. The DNN approach is shown in black, doppler lidar (Sivaraman and Zhang. 2021)  
 1001 in yellow, ceilometer (Zhang et al. 2022) in pink, micro-pulse lidar (MPL, Sawyer and

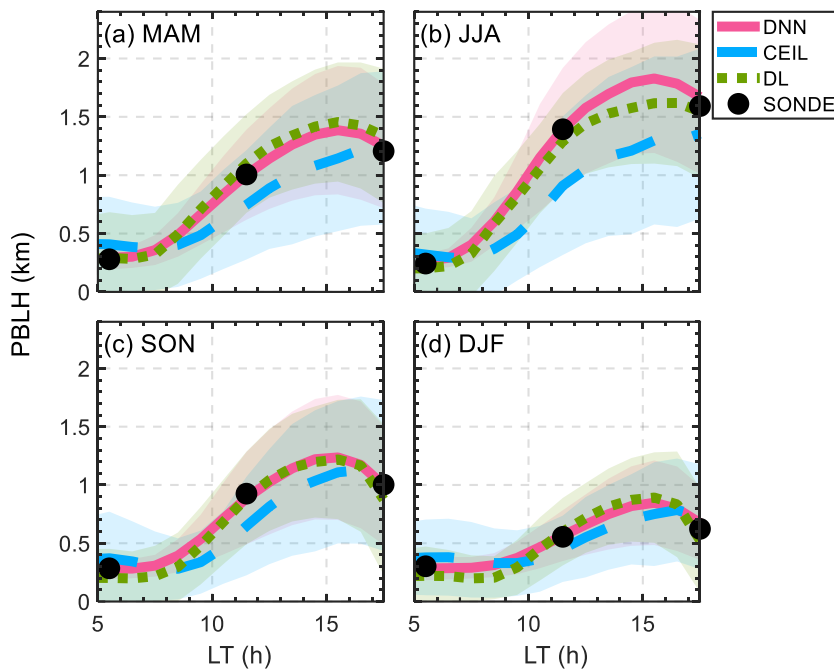
1002 Li. 2013) in light red, and Raman lidar (Ferrare. 2012) in dark red. DNN model is  
 1003 trained during 1994-2016. Individual MAE values for DNN are represented by gray  
 1004 dots, while the solid lines denote the smoothed MAE for each method with a 2-year  
 1005 smooth window.



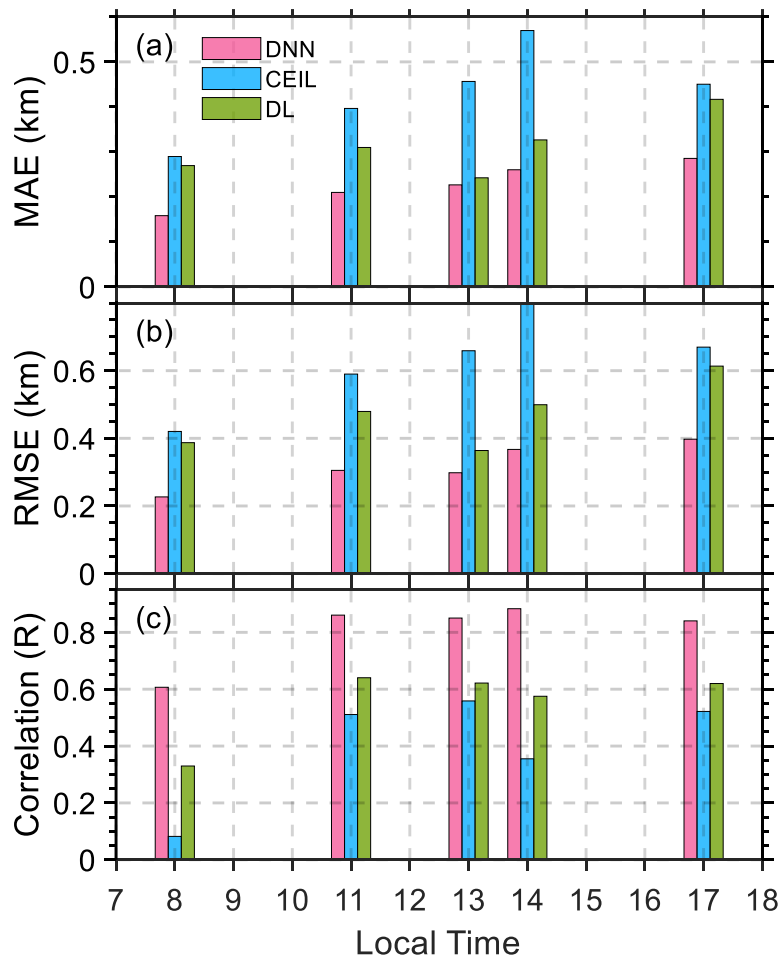
1006

1007 **Figure 5:** Scatter plots comparing observed radiosonde (SONDE) PBLH with estimates  
 1008 from the machine learning model and lidar observations. Panels (a) and (b) show the  
 1009 PBLH estimated by the deep neural network (DNN) during the trained period (1994-  
 1010 2016) and the untrained period (2017-2020), respectively, with corresponding  
 1011 correlation coefficients (R) and mean absolute errors (MAE). Panels (c) and (d) display  
 1012 comparisons of Sonde PBLH with ceilometer (CEIL) and doppler lidar (DL) derived

1013 PBLH, respectively. The color gradient indicates the normalized density of data points,  
 1014 while the solid black line represents the line of best fit and error bars indicates the mean  
 1015 and standard deviations for each bin.

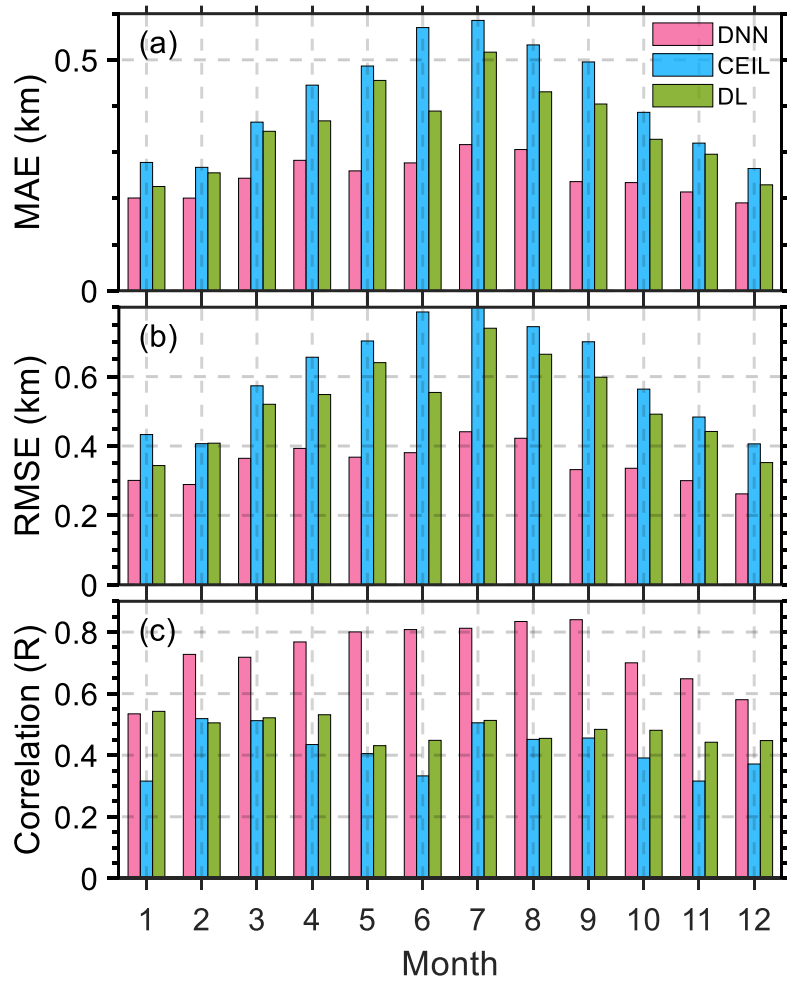


1016  
 1017 **Figure 6:** Seasonal-averaged daytime evolution of planetary boundary layer height  
 1018 (PBLH) derived from various methods. The panels represent the mean PBLH values  
 1019 throughout the day for different seasons: (a) March-April-May (MAM), (b) June-July-  
 1020 August (JJA), (c) September-October-November (SON), and (d) December-January-  
 1021 February (DJF). The PBLH values estimated by the deep neural network (DNN) are  
 1022 shown in red, ceilometer (CEIL) estimates in blue, Doppler lidar (DL) in green, and  
 1023 observed radiosonde (SONDE) data in black. Shaded areas around the lines indicate the  
 1024 standard deviations within each method.



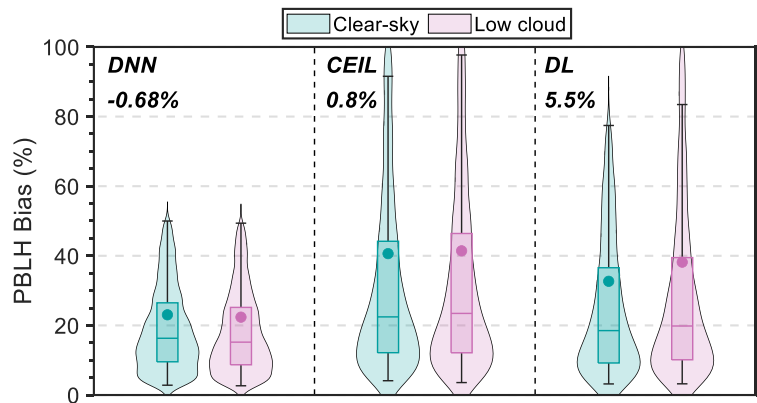
1025

1026 **Figure 7:** Diurnal variations in the performance metrics for estimating PBLH using  
 1027 different datasets. (a) Shows the correlation coefficient (R), (b) represents the root mean  
 1028 square error (RMSE), and (c) depicts the mean absolute error (MAE) at various local  
 1029 times throughout the day. The deep learning neural network (DNN) estimates are in  
 1030 blue, ceilometer (CEIL) derived estimates are in pink, and doppler lidar (DL) estimates  
 1031 are in green. Note that these biases metrics are calculated using SONDE PBLH as the  
 1032 standard. The availability of SONDE data for different hours is detailed in Table 2.



1033

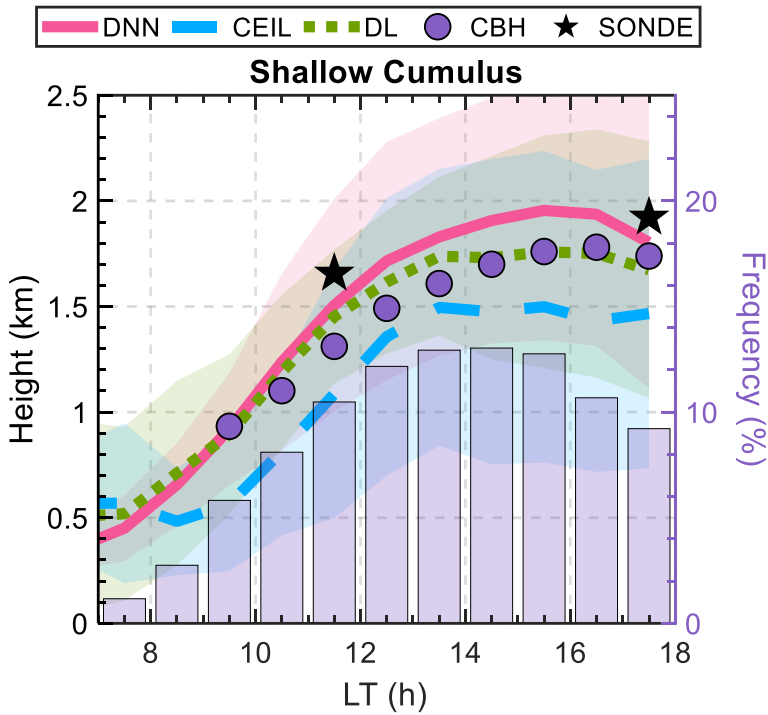
1034 **Figure 8:** Similar to Figure 7, but for MAE, RMSE, and R for different month.



1035

1036 **Figure 9:** Comparative analysis of PBLH estimation bias under clear-sky and low cloud  
 1037 conditions for various methods. Bias percentages are computed as the absolute bias  
 1038 normalized by the mean PBLH for each condition, with the number above each method  
 1039 indicating the difference in bias between low cloud and clear-sky scenarios. The  
 1040 boxplots detail the 10th, 25th, 50th, 75th, and 90th percentiles, while shaded areas in  
 1041 violin plots illustrate the distribution of dataset biases. The dots indicate the mean value  
 1042 for each condition.

1043

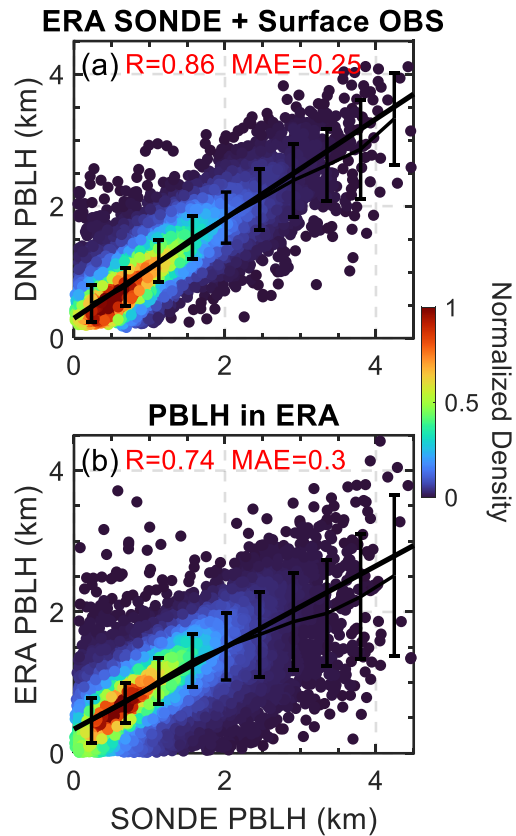


1044

1045 **Figure 10:** Daytime evolution of planetary boundary layer height (PBLH) derived from  
 1046 various methods under the shallow cumulus condition. PBLH values estimated by the  
 1047 deep neural network (DNN) are shown in red, ceilometer (CEIL) estimates in blue,  
 1048 Doppler lidar (DL) in green. Observed radiosonde (SONDE) data are represented by  
 1049 black stars. Purple bars show the relative frequency of shallow cumulus occurrences  
 1050 throughout the day, while purple dots mark the corresponding cloud-base heights  
 1051 (CBH). Shaded areas around each line reflect the standard deviations for each method.

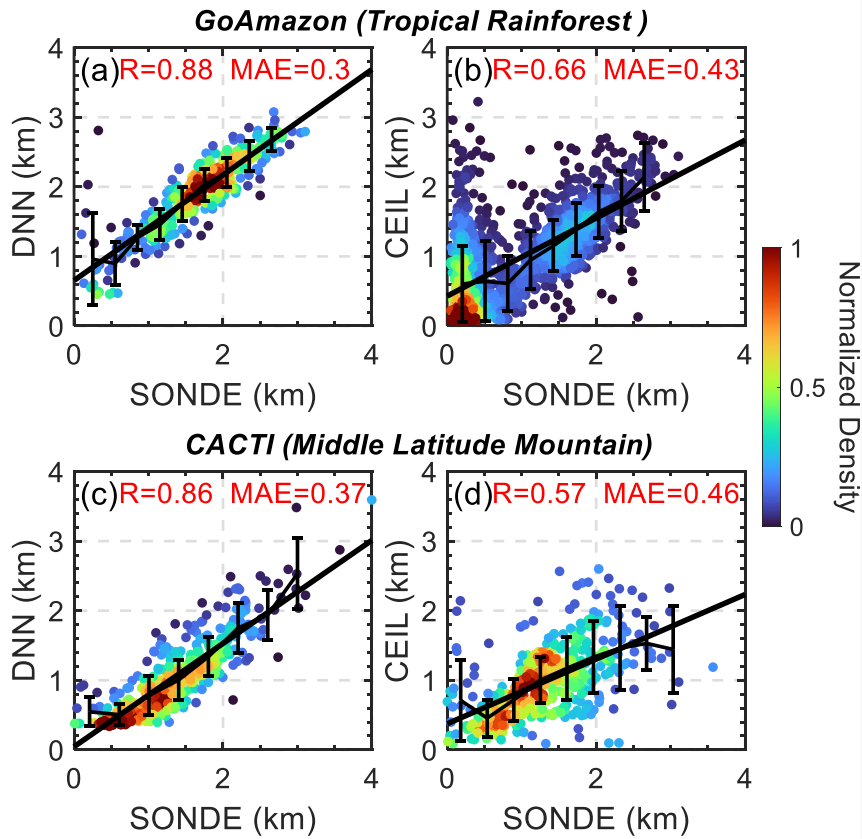
1052



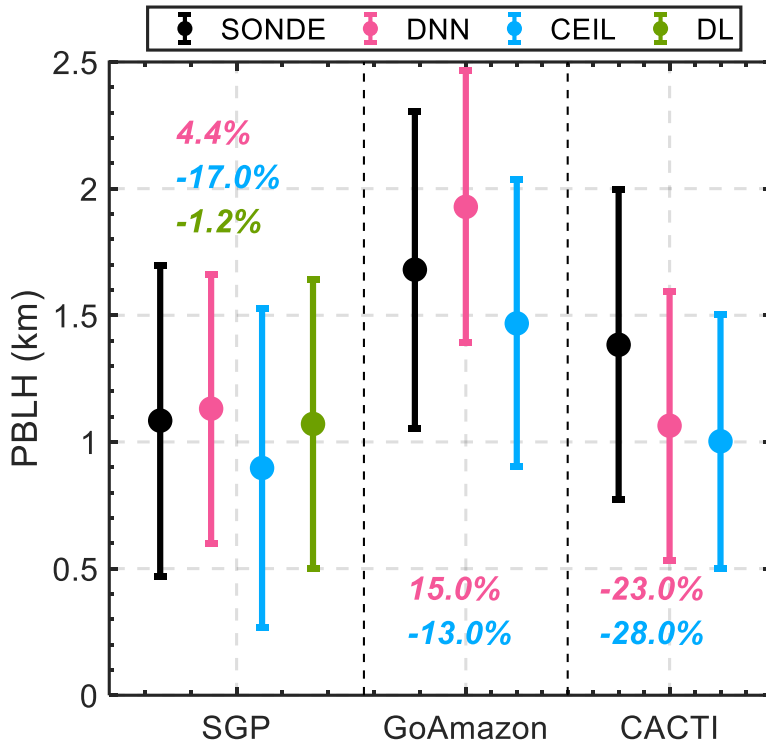


1053

1054 **Figure 1011:** Scatter plots comparing SONDE PBLH with estimates from the DNN  
 1055 and ERA-5. (a) The comparison between observed SONDE PBLH and estimates from  
 1056 the DNN model, which utilizes morning temperature profiles (5 LT) from ERA-5 (ERA  
 1057 Profile) and observed surface meteorological data (surface OBS) as inputs. (b) The  
 1058 correlation comparison observed SONDE PBLH and PBLH model outputs from the  
 1059 ERA-5 datasets. The color gradient in both panels represents the normalized density of  
 1060 data points, while the solid black line indicates the linear regression, and the error bars  
 1061 denote the mean and standard deviations for each bin.



1062  
 1063 **Figure 1412:** Validation of the DNN trained over the SGP for the GoAmazon (Tropical  
 1064 Rainforest) and CACTI (Middle Latitude Mountain) field campaigns. Panels (a) and (c)  
 1065 illustrate the correlation ( $R$ ) and mean absolute error (MAE) between DNN predictions  
 1066 and SONDE observations for GoAmazon and CACTI, respectively. Panels (b) and (d)  
 1067 show the performance of ceilometer (CEIL) derived PBLH compared to SONDE for  
 1068 the same campaigns. The color gradient indicates the normalized density of data points,  
 1069 while the solid black line represents the line of best fit and error bars indicates the mean  
 1070 and standard deviations for each bin.



1071

1072 **Figure 1213:** Comparative PBLH mean (dots) and standard deviations (error bars)  
 1073 across ARM sites (SGP, GoAmazon, and CACTI). The datasets are derived from  
 1074 radiosonde (SONDE, in black), the DNN model (in pink), ceilometer (CEIL, in blue),  
 1075 and Doppler lidar (DL, in green), respectively. Noted the DL-derived PBLH is only  
 1076 available at the SGP. The percentages in various colors denote the differences in PBLH  
 1077 means derived from the DNN, CEIL, and DL methods relative to SONDE observations.  
 1078 To mitigate sampling bias, these mean values and standard deviations are computed  
 1079 exclusively for intervals where all instruments have concurrently available data.